The Thesis Committee for Lauren Elizabeth Becker
Certifies that this is the approved version of the following thesis:

The Seismic Response to Fracture Clustering: A Finite Element Wave Propagation Study

APPROVED BY
SUPERVISING COMMITTEE:

Supervisor:

Kyle T. Spikes

Robert H. Tatham

Mrinal K. Sen

The Seismic Response to Fracture Clustering: A Finite Element Wave Propagation Study

by

Lauren Elizabeth Becker, B.S.

Thesis

Presented to the Faculty of the Graduate School of
The University of Texas at Austin
in Partial Fulfillment
of the Requirements
for the Degree of

Master of Science in Geological Sciences

The University of Texas at Austin
May 2014

Dedication

I dedicate this thesis to my infinitely loving and supportive family, Teresa, Fred and Lindsay Becker, and to my other half, Mark Eberhard. Without their encouragement, guidance, and inspiration, I could have not gotten to where I am today. Thank you for supporting me in every way.

Acknowledgements

First I would like to thank Dr. Kyle Spikes for giving me the opportunity to work on this project under his supervision. His knowledge, expertise, and guidance were invaluable to this project and I am very grateful to have had him as my adviser. Without his patience and attentiveness, this thesis would not have been possible. This thesis would also not have been possible without the hard work of Dr. Jonas De Basabe. His SWP3D modeling software was the backbone of this project and I was fortunate to have been able to use it. I would also like to thank Thomas Hess for his technical support, savvy, and eagerness to help with any and all problems that arose during my time at the Jackson School.

I am grateful to Dr. Robert Tatham who laid the groundwork for my knowledge in exploration geophysics. His passion for the subject motivated me to seek out research opportunities that lead to this thesis. Dr. Mark Cloos, Dr. Luc Lavier, and Dr. Clark Wilson were also very influential undergraduate professors who taught me the skills needed to complete this research and who inspired me to continue my education. I would also like to thank Dr. Mrinal Sen for being open to discussion and sharing his knowledge on numerical modeling with me.

Finally, I would like to thank my fellow EDGER Forum students and my officemates for enriching my academic experience. In particular, I would like to thank Meijuan Jiang and Russell Carter for their mentorship, Debanjan Datta for his help with any and all software I used, and Sarah Coyle, Jacqui Maleski, Qi Ren, Han Liu, Karl Sletten, and Chris Linick for creating a fun and enjoyable work environment that kept me sane throughout the past two years.

Abstract

The Seismic Response to Fracture Clustering: A Finite Element Wave Propagation Study

Lauren Elizabeth Becker, M.S. Geo. Sci.
The University of Texas at Austin, 2014

Supervisor: Kyle T. Spikes

Characterizing natural and man-made fracture networks is fundamental to predicting the storage capacity and pathways for flow of both carbonate and shale reservoirs. The goal of this study is to determine the seismic response specifically to networks of fractures clustered closely together through the analysis of seismic wavefield scatter, directional phase velocities, and amplitude attenuation. To achieve this goal, finite element modeling techniques are implemented to allow for the meshing of discontinuous fracture interfaces and, therefore, provide the most accurate calculation of seismic events from these irregular surfaces.

The work presented here focuses on the center layer of an isotropic model that is populated with two main phases of fracture network alteration: a single large-scale cluster and multiple smaller-scale clusters. Phase 1 first confirms that the seismic response of a single idealized vertically fractured cluster is distinct crosscutting energy within a seismogram. Further investigation shows that, as fracture spacing within the cluster decreases, the depth at which crosscutting energy appears exponentially increases, placing

it well below the true location of the cluster. This relationship holds until 28% of the fractures are moved from their uniformly spaced locations to random locations within the cluster. The vertical thickness of the cluster has little effect on the location or strength or the crosscutting signature.

Phase 2 shows that, although clusters of more randomly spaced fractures mask crosscutting energy, a marked decrease in amplitude coinciding with a bend in the wavefront produces a heterogeneous anisotropic seismic response. This amplitude decay and heterogeneous anisotropy is visible until cluster spacing drops below one half of the wavelength or the ratio of fractured material to matrix material within a cluster drops below 37%. Therefore, the location of an individual fracture cluster can be determined from the location of amplitude decay, heterogeneous anisotropy, and crosscutting energy. Furthermore, the density of the cluster can be determined from the degree of amplitude decay, the angle of heterogeneous anisotropy, and the depth of cross-cutting energy. These relationships, constrained by limits on their detectability, can aid fracture network interpretation of real seismic data.

Table of Contents

List of Figures

Chapter 1: Introduction

MOTIVATION

Characterizing natural and man-made fracture networks is essential for the optimization of current production and for the discovery of new oil and gas reserves. Unconventional resources are the first to come to mind when discussing fractures due to the explosion in popularity of hydraulic fracturing for enhanced hydrocarbon recovery. Hydraulic fracturing creates new fracture networks to increase permeability in shale reservoirs where hydrocarbons would otherwise be unable to flow. Although this production technology relies on newly created fractures, understanding in-situ fracture locations and orientations allows the production team to optimize their fracturing efforts. A stage can be planned so that it either avoids large faults that funnel fracturing fluids out of the desired area, minimizing the effects of the fracturing process, or targets hydraulic fracturing perpendicular to natural fracture clusters to increase the areal reach of the stage.

Most recently, conventional reservoirs have begun to benefit from knowledge on natural fracture networks as well. In reservoirs, such as carbonate rocks, with a tight or highly variable rock matrix, natural fractures can fulfill the same purpose as in unconventional reservoirs and help drain hydrocarbons through areas with decreased permeability. Dense clusters of fractures, in particular, have been reported to locally increase permeability well above 10 Darcy in Middle Eastern carbonates (Singh et al., 2008). Large swaths of natural fracture clusters formed during tectonic folding can also enhance porosity by increasing the porous volume for hydrocarbon accumulation in anticlinal structures. Therefore, characterizing natural fracture networks is fundamental in predicting the storage capacity and pathways for flow in the reservoir types that are most promising to meet future energy demands.

Many different observations provide pieces of information on subsurface fracture attributes. Borehole measurements, such as formation micro-imaging, flowmeter readings, or conductivity logging, can provide in-situ data on fracture orientation, connectivity, and openness (Figure 1.1, left). Unfortunately, this information is limited to the areal extent of the borehole or the depth of investigation of the logging tool, which makes these techniques less than ideal for 3D reservoir characterization. Seismic surveying, by contrast, allows for broad coverage over a large area, but it only provides relatively low resolution elastic properties, such as velocity anisotropy or excess matrix compliance, that are indirectly related to rock properties (Figure 1.1, right). Outcrops are an attractive intermediate-scale choice to formulate concepts of fracture networks because of their visible small-scale features, relatively large scale extents, and accessibility (Marrett et al., 2007). However, establishing clear relationships between uplifted and weathered outcrops and subsurface formations of production interest remains difficult (Figure 1.1, center). As a result of this variety of techniques for gathering data on fracture attributes, we are left with mismatched pieces of information that are problematic to join together in terms of scale and resolution.

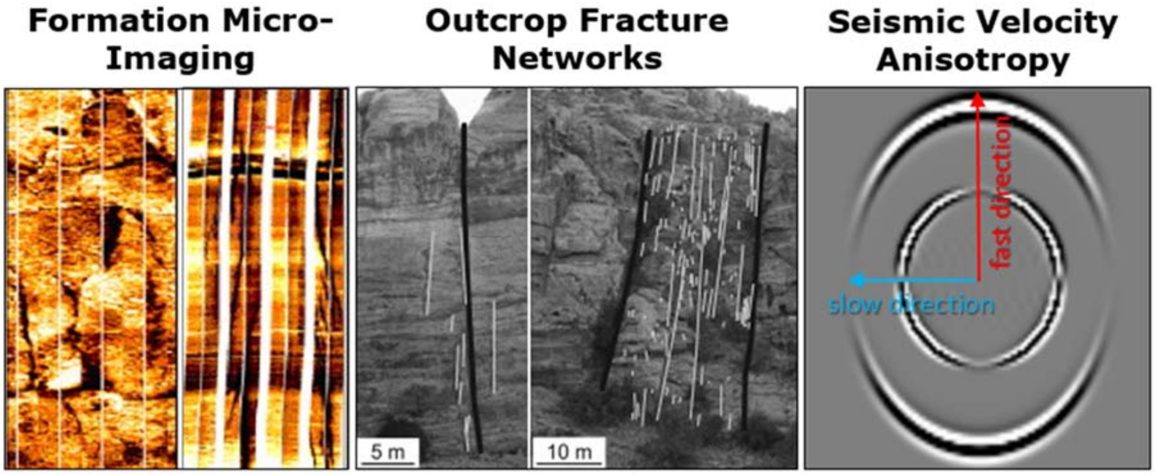
Formation Micro-Imaging

Outcrop Fracture Networks

Seismic Velocity Anisotropy

Figure 1.1 (Modified from Xiao and Li, 2011 - left, and Strijker et al., 2012 - center) Current techniques for gaining information on subsurface fracture attributes. Formation Micro Imaging produces a pseudo-image of the borehole wall that allows for a visual determination of the orientation and openness of fractures intersecting the borehole only (left). Outcrops provide a laterally continuous surface for studying the interplay of small and large scale fracture parameters but it is difficult to separate the effects of uplift and weathering from original subsurface features (center). Seismic velocity data has broad coverage over a reservoir, but only provides an indirect assessment of fracture network orientation and compliance from measurements of velocity anisotropy (right).

Numerical modeling is the key that connects all the observed levels and scales of information about fractures into a single interpretable package. Specifically, wave propagation modeling is most advantageous in that it is based on the elastic wave equation for heterogeneous media and, therefore, can simulate direct waves, primary and multiply reflected and transmitted waves, converted waves, diffracted waves and critically refracted waves (De Basabe, 2009). By building a numerical model based on fracture characteristics taken from boreholes and related outcrops, it is possible to thoroughly study the seismic response of realistic fracture patterns in a reservoir of interest.

This approach of calibrating a model to a specific reservoir is much preferred over the use of arbitrary or geometrically convenient fracture shapes and patterns. Given an expected range of fracture apertures, lengths, and density distributions, numerical modeling can be used to study how variations in these parameters affect seismic energy attenuation (Hudson et al. 1996; Dasgupta and Clark, 1998; Chichinina et al., 2006) and wavefield scattering (Leary and Abercrombie, 1994; Pearce, 2003; Vlastos et al., 2003; Willis et al., 2004, 2006). The anticipated patterns of attenuation and scattering can then be used to better distinguish areas of interest in a reservoir containing favorable fracture densities and economic fills from areas comprised of less promising features.

OBJECTIVES

The objective of this study is to expand on previous investigations that analyzed the seismic response to fracture networks by modeling more realistic fracture parameters and by comparing the results in a more quantitative manner. Previous studies have used finite difference methods to model and thoroughly investigate wavefield patterns produced from simple fracture networks with evenly spaced, un-naturally wide, solely gas filled fractures (Vlastos et al., 2003; Xu, 2011; Hou et al., 2012). Their conclusions qualitatively state that little information can be gained when fractures are spaced below seismic resolution. Although it is a geophysical principle that seismic waves will experience interference if objects are spaced less than one fourth the seismic wavelength (Tatham and McCormack, 1991), this has not halted studies of thin bed thickness estimation and wedge model resolution (Marfurt and Kirlin, 2001; Nowak et al., 2008; Spikes, 2009).

These previous studies on fractures are, instead, hampered by their chosen modeling methods. Older modeling techniques, such as effective medium and finite difference methods, are greatly limited in their ability to discern fracture parameters due to their oversimplified representation of realistic fractured media. To achieve the first portion of my objective, I implement better suited finite element modeling methods that allow for more accurate representation of fractured media. I have chosen to broaden this study further to include fracture networks with closely spaced fractures, smaller vertical-scale fractures, and non-uniformly spaced fractures to simulate fracture clustering. These additions are necessary steps to add complexities that we know exist in the subsurface from cores and borehole images.

Finite Difference studies have also obstructed pertinent conclusions by over simplistically comparing the results of models containing differing fracture network attributes. For example, it has been documented numerous times that the seismic response to fractures with uniform spacing ranging from the seismic wavelength to seismic resolution is the formation of a crosscutting pattern in seismograms (Pearce, 2003; Vlastos et al., 2003; Burns et al., 2007; Xu, 2011). None of these studies have tested the effects of fracture density, length, or non-uniform spacing on the formation of this pattern. Without this information, it is unclear if crosscutting energy could be observed in real data. To achieve the second portion of my objective, I vary parameters of the idealized networks and measure the locations, extent, and intensity of crosscutting energy until it is no longer discernible. By testing the sensitivity of fracture-related wavefield events to the fracture parameters that create them, I am able to discern the seismic detectability of fracture network attributes. Therefore, I am able to more reliably point interpreters in the right direction to look for hints of the presence of fractures in a seismic volume.

THESIS ORGANIZATION

This thesis is divided into six chapters. Chapter 1 provides a brief overview of the motivation behind this project, the objectives accomplished, and the software utilized to complete this project. Chapter 2 covers the fundamentals of the phenomenon of fracture scattering attenuation, which builds a framework for the rest of the chapters in this study. Chapter 3 discusses the theory behind modeling fractured media and numerically propagating a seismic wave through that medium. Chapter 4 outlines the calculations and reasoning that go into choosing variable values within the SWP3D software and covers the methodology of modeling individual fracture attributes phase by phase. Chapter 5 details the results of fracture network attribute alteration phase by phase and subsections are used further analyze the detectability of relationships between seismic events and fracture network parameters. Lastly, chapter 6 covers discussions and conclusions from this work.

SOFTWARE UTILIZED

In this work, four main software were used:

- **Seismic Wave Propagation 3D** (SWP3D) is an open source software managed by the EDGER Forum at the University of Texas at Austin. I use this program to create model meshes and to numerically propagate a wave through the model.
- **Seismic Unix** (SU) is an open source software package used for seismic data processing managed by the Center for Wave Phenomena at Colorado School of Mines. I use this program primarily for data visualization and secondarily for minor data processing.
- **Matlab** is a commercial software for mathematical calculations. I use this program to ease the creation of SWP3D input files and calculation of various parameters.

- **Host2sgy** is an open source software managed by the University of Texas Institute for Geophysics. I use this program to convert the binary files generated by SWP3D into SEGY files that are readable using other software.

Chapter 2: Fundamentals of Fracture Scattering Attenuation

SEISMIC RESPONSE TO AN ELASTIC INTERFACE

The work presented here is fundamentally based on the theory of reflection, diffraction, and transmission. A seismic wave is, by definition, an elastic wave produced when particles in a certain region are set in motion by a mechanical perturbation (Sheriff and Geldart, 1995). The elastic wave is the resultant motion within the medium to restore the particles to their original position. Seismic waves will propagate directly through a medium until a change in acoustic impedance, defined as the product of a specific medium's velocity and density, is reached. Therefore, the response of the seismic wave to an interface separating two mediums is given by:

$$R = \frac{AI_1 - AI_2}{AI_2 + AI_1} \tag{2.1}$$

$$T = \frac{2 * AI_1}{AI_2 + AI_1} \tag{2.2}$$

where R is the seismic wave's reflectivity response, T is the transmitivity response, AI_1 is the acoustic impedance of the upper layer, and AI_2 is the acoustic impedance of the lower layer (Mavko et al., 2009).

The Components of a Seismic Wavefield

Elastic seismic waves are separated into two categories based on the motion of particle restoration during wave propagation and during reflection and transmission off of an interface. Waves with particle motion parallel to the direction of wave propagation are called compressional, or P-waves, and particle motion is further confined to the vertical plane in which the source of the perturbation acts (Figure 2.1, left). Waves with particle motion perpendicular to the propagation direction are called shear, or S-waves, and are divided into two categories: those with particle motion perpendicular to the vertical source plane, called shear horizontal or SH-waves (Figure 2.1, center), and those with particle motion parallel to the vertical source plane, called shear vertical or SV-waves (Figure 2.1, right).

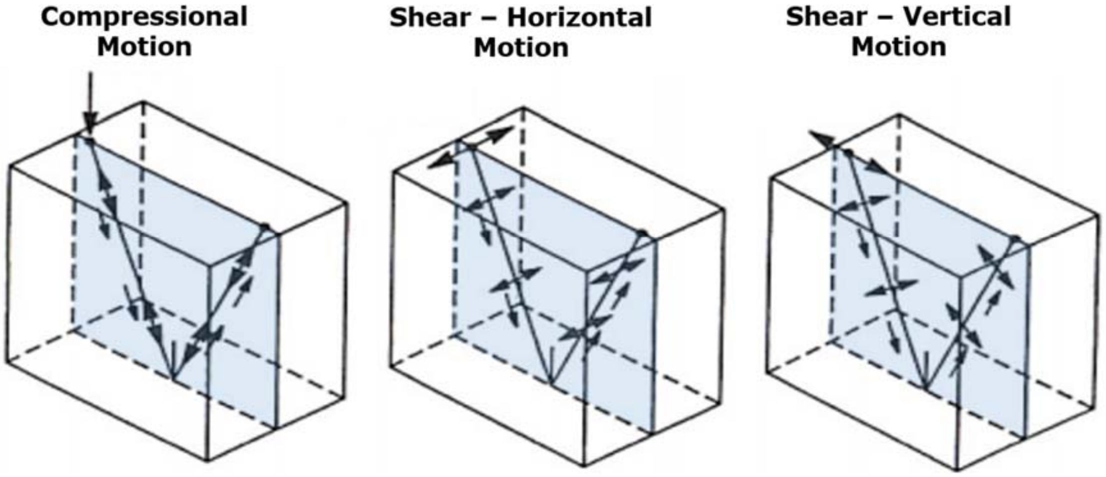

Figure 2.1: (Modified from Tatham and McCormack, 1991) Diagram of the different categories of seismic waves. Compressional seismic waves contain particle motion that is parallel to the direction in which the seismic wave propagates and that is confined to the vertical plane defined by the source of wave motion (left). Shear seismic waves contain particle motion that is perpendicular to the direction in which the seismic wave propagates. Shear Horizontal, or SH-waves, are further defined as having particle motion that is confined to a plane perpendicular to the vertical source plane (center), while Shear Vertical, or SV-waves, are defined as having particle motion that is confined to the vertical source plane (right).

Compressional Wave Mode Conversion

Traditionally seismic sources that generate compressional waves are used in hydrocarbon exploration because P-waves can propagate in fluids and are easy to generate (Stewart et al., 2002). Therefore, when a compressional seismic wave encounters an interface separating isotropic layers of differing acoustic impedance, equations 2.1 and 2.2 indicate that the resulting wavefield should consist of a reflected P-wave and a transmitted

P-wave. However, two other wavefield components are generated: a reflected SV-wave and a transmitted SV-wave at non-normal angles of incidence. This phenomenon is known as mode conversion and is a result of the interaction of the wave with the interface. As stated earlier, P-waves have particle motion that is parallel to the direction of wave propagation, and that is confined to the vertical source plane. When a P-wave comes in contact with a surface at non-normal incidence, particle motion will be at an angle to the surface and will decompose into two perpendicular directions upon reflecting or transmitting, forming P-waves and SV-waves (Tatham and McCormack, 1991). SH-waves are not generated from mode conversion because particle motion begins and remains parallel to the vertical source plane.

Seismic Wave Decomposition

The partitioning of the four components within a seismic wavefield are governed by two fundamental equations: Snell's Law and Zoeppritz Equations. Snell's Law governs the geometric partitioning of the wave by using the P-wave incident angle θ_{p1}, upper layer compressional velocity V_{p1} and shear velocity V_{s1}, and lower layer compressional velocity V_{p2} and shear velocity V_{s2}:

$$\frac{\sin\theta_{\mathrm{P1}}}{V_{\mathrm{P1}}} = \frac{\sin\theta_{\mathrm{S1}}}{V_{\mathrm{S1}}} = \frac{\sin\theta_{\mathrm{P2}}}{V_{\mathrm{P2}}} = \frac{\sin\theta_{\mathrm{S2}}}{V_{\mathrm{S2}}} \tag{2.3}$$

where θ_{p2} is the P-wave transmission angle, θ_{s1} is the mode-converted S-wave reflection angle, and θ_{s2} is the mode-converted S-wave transmission angle (Sheriff and Geldart, 1995). Zoeppritz Equations govern the energy partitioning of the wave by building upon Snell's Law. Using the angles θ_{p2}, θ_{s1}, and θ_{s2} calculated in equation 2.3, the upper and lower layer velocities V_{p1}, V_{s1}, V_{p2}, and V_{s2}, and the upper and lower layer densities, Zoeppritz Equations can be used to solve for the amplitudes of the reflected P-wave R_p, reflected S-wave R_s, transmitted P-wave T_p, and transmitted S-wave T_s:

$$\begin{bmatrix} \cos\theta_{\mathrm{P1}} & -\sin\theta_{\mathrm{S1}} & \cos\theta_{\mathrm{P2}} & \sin\theta_{\mathrm{S2}} \\ \sin\theta_{\mathrm{P1}} & \cos\theta_{\mathrm{S1}} & -\sin\theta_{\mathrm{P2}} & \cos\theta_{\mathrm{S2}} \\ Z_1\cos 2\theta_{\mathrm{S1}} & -W_1\sin 2\theta_{\mathrm{S1}} & -Z_2\cos 2\theta_{\mathrm{S2}} & -W_2\sin 2\theta_{\mathrm{S2}} \\ \frac{V_{\mathrm{S1}}}{V_{\mathrm{P1}}}W_1\sin 2\theta_{\mathrm{P1}} & W_1\cos 2\theta_{\mathrm{S1}} & \frac{V_{\mathrm{S2}}}{V_{\mathrm{P2}}}W_2\sin 2\theta_{\mathrm{P2}} & -W_2\cos 2\theta_{\mathrm{S2}} \end{bmatrix} \begin{bmatrix} R_{\mathrm{P}} \\ R_{\mathrm{S}} \\ T_{\mathrm{P}} \\ T_{\mathrm{S}} \end{bmatrix} = \begin{bmatrix} \cos\theta_{\mathrm{P1}} \\ -\sin\theta_{\mathrm{S1}} \\ -Z_1\cos 2\theta_{\mathrm{S1}} \\ \frac{V_{\mathrm{S1}}}{V_{\mathrm{P1}}}W_1\sin 2\theta_{\mathrm{P1}} \end{bmatrix} \tag{2.4}$$

where $Z_1$and Z_2 are the upper and lower layer compressional impedance, respectively, and W_1 and $W_1$are the upper and lower layer shear impedance.

To better illustrate the insights conveyed in equations 2.3 and 2.4, Figure 2.2 visually represents incident compressional wave geometric partitioning in the left column and energy partitioning in the right column. The top row of Figure 2.2 focuses on the case of an impedance increase, whereby an interface separates a shallow, lower velocity and density layer from a deeper, higher velocity and density layer. This is the most common case found in the subsurface due to increased effects of compaction with increased depth. It is evident from the top left image that the P-reflected wave travels upward from the interface at the same angle from vertical as the incident P-wave because V_{p1} throughout the upper layer is constant. The mode converted S-reflected wave travels upward at an angle less than that of the P-reflected wave because $V_{s1} < V_{p1}$.

Given that $V_{p1}, V_{s1} < V_{p2}, V_{s2}$, the angle of transmission is greater than the angle of reflection, and the P-transmitted wave travels downward from the interface at a larger angle from vertical than the P-reflected wave. The S-transmitted wave travels downward at an angle greater than that of the S-reflected wave but smaller than that of the P-transmitted wave. Although not clear from the top left image in Figure 2.2, as the angle of incidence increases, the angles from vertical at which the P-transmitted and S-transmitted waves propagate increases. This relationship holds until the critical angle, of 30 degrees in this case ($V_{p1}/V_{p2} = 0.5$), is reached and refraction along the interface takes place. From the top right image in Figure 2.2, it is evident that the majority of seismic energy is partitioned into the P-transmitted wave until large angles of incidence are reached, at which time the P-reflected wave begins to dominate. It is also clear that mode conversion does not take place at normal incidence and that S-wave components never contain a significant amount of seismic energy.

The bottom row of Figure 2.2 focuses on the opposite case of an impedance decrease, whereby an interface separates a shallow, higher velocity and density layer from a deeper lower velocity layer. Though not a common scenario, anomalies such as an increase in the ratio of void to solid space in the deeper layer relative to the shallower layer can produce such an effect. From the bottom left image, it is evident that the P-reflected and S-reflected waves do not change their relative geometry because the upper layer's properties have not changed. However, the angles from vertical at which the P-transmitted and S-transmitted waves travel downward from the interface are decreased due to the decrease in impedance of the lower layer and the angles decrease further as the angle of incidence increases.

From the bottom right image in Figure 2.2, it is clear that the P-transmitted component of the wave contains the entirety of seismic energy until moderate angles of incidence are reached. As the incidence angle approaches 30 degrees, P-transmitted wave amplitude sharply decreases to zero. Mode conversion begins for both reflected and transmitted components and is marked by a pronounced spike in S-wave energy. Mode conversion tapers off as larger offsets are reached, and seismic energy is then preferentially partitioned into the P-reflected wave, whose amplitude increases significantly as the angle of incidence increases.

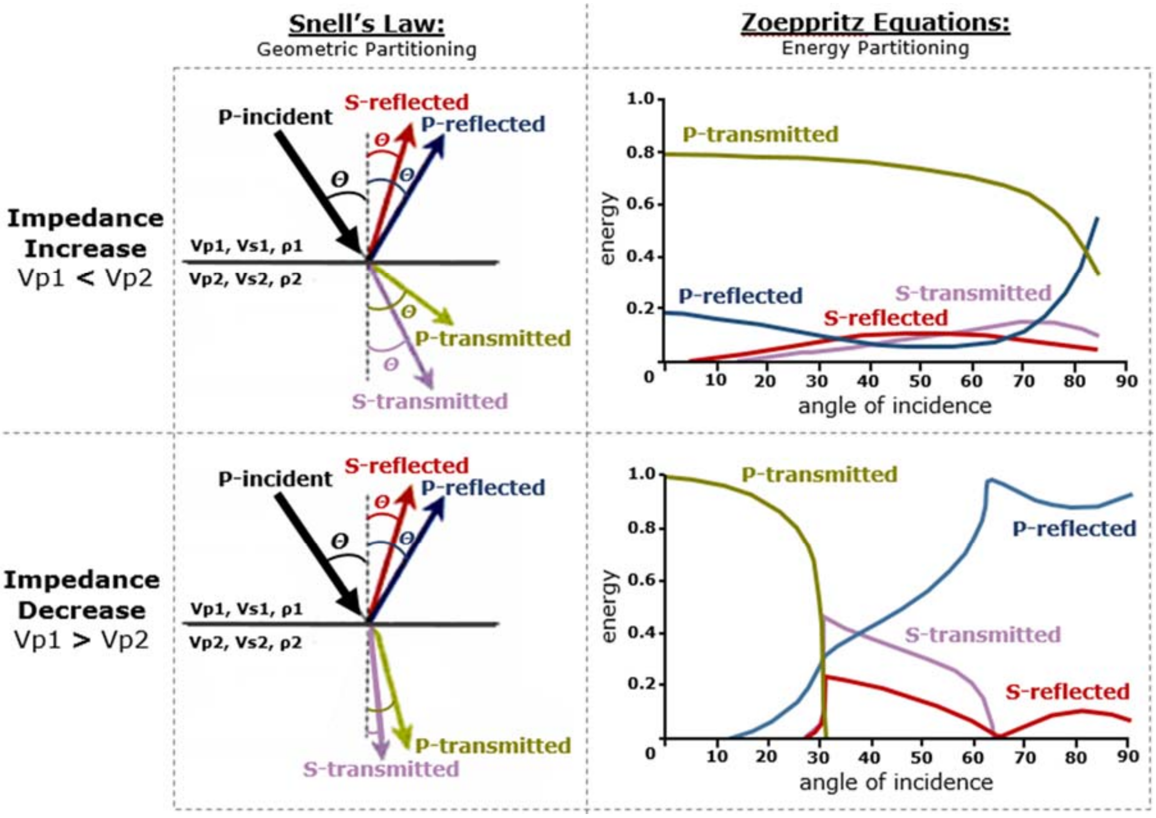

Figure 2.2: (Modified from Sheriff and Geldart, 1995) A visual representation of the equations governing the seismic response to an interface separating layers of differing acoustic impedances. When the interface is defined by an increase in impedance, Snell's Law shows that the compressional and mode converted shear waves' angles of transmission increase as the angle of incidence increases. The Zoeppritz Equations show that the majority of seismic energy is partitioned into the compressional transmitted wave until large offsets are reached. When the interface is defined by a decrease in impedance, Snell's Law shows that the compressional and mode converted shear waves' angles of transmission decrease as the angle of incidence increases, and Zoeppritz Equations show that the compressional transmitted wave only contains the majority of seismic energy at small offsets and compressional reflected waves dominate thereafter.

Layered and Irregular Interfaces

The theory outlined above defines the seismic response to the textbook case of an interface separating two uniform layers. To restate the main points, at normal incidence and moderately increasing impedance across the interface, the majority of seismic energy is transmitted directly through the layered interface, as determined by Zoeppritz equations. Only a small portion of the energy is reflected back toward the surface (Figure 2.3, left). This is a key concept behind seismic surveying. If all of the energy is reflected back to the surface at shallow depths, no energy would propagate downward and provide information on reservoir-depth intervals. As the angle of incidence increases, due either to relative positioning of the source and interface of interest or to the dip of the interface, the amount of relative energy partitioned into transmitted waves decreases and reflected energy becomes stronger.

The seismic response of acoustic impedance contrasts at irregular interfaces, such as vertical fractures, is not as well understood (e.g., Schultz and Toksoz, 1996). Two factors strongly differentiate fractured interfaces from layered interfaces: (1) fractures are narrow, elongate features with large curvature changes at each end, and (2) fractures are normally associated with a strong decrease in impedance due to low density and velocity fluid infill. Therefore, at normal incidence, most of the seismic energy should be transmitted through the fracture due to the decrease in impedance (Figure 2.2, bottom). However, the vertical tip of the fracture acts as a point source, diffracting wave energy in all directions (Figure 2.3, right).

As the angle of incidence increases, the seismic wavefield can interact with the planar side of the fracture, but the sharp decrease in transmitted-wave energy as a function of incidence angle again prevents much of the seismic energy from passing through the fracture. Instead, the wavefield is continuously reflected back and forth at sharp angles off of the length of the faces of the fractures (Figure 2.3, right). With each reverberation, mode conversion decreases the amplitude of the reflected waves until only faint scatter is left to exit the fractured interval (Schultz and Toksoz, 1996; Daley et al., 2002; Nakagawa et al., 2003). These processes of wavefield energy loss and amplitude decay that occur during the wave's traverse of the fractured interval are called scattering attenuation (Aki and Chouet, 1975). Because of this scattering attenuation, imaging fractured intervals and layers lying below these intervals is a difficult process.

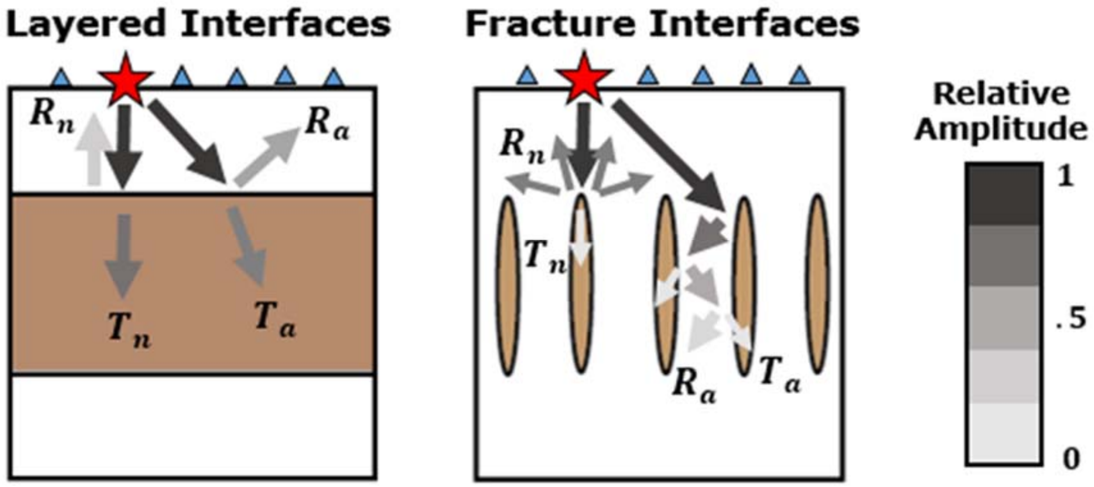

Figure 2.3: An illustration of reflection, diffraction, and transmission at different interfaces. As energy, represented by the shaded arrows, propagates from a seismic source, represented by the red star, encounters an impedance contrast, the waves are reflected off of this interface and transmitted through this interface. The normal incidence reflections and transmissions are marked with an R_n and T_n, respectively, and the angle-dependent reflections and transmissions are marked with an R_a and T_a, respectively. When the interface separates layered media (left), the waves reflect and transmit in a common manner. When the interface is a fracture (right), normal incidence waves are scattered in all directions causing a diffraction instead of a reflection, and little energy is transmitted through the fracture. Waves encountering fractured interfaces at an angle are reflected between the fractures, and little energy is transmitted through the fracture.

UTILITY OF FRACTURE WAVEFIELD EVENTS

Scattering of seismic waves at fracture interfaces is typically viewed only as unfavorable noise in seismic data. Scattering attenuation is lumped together with backscattering, and appropriate processing steps are applied to mask or remove these effects. Contrary to this view point, scattering from fractures is not random noise because fractures themselves are not random features. Fractures most commonly occur in regular fracture sets that are restricted to brittle rock units and have ranges of fracture lengths, fracture spacings, and specific orientations (Ozkaya et al., 2003). This regularity within a particular set and, therefore, the regularity of resulting wavefield features allows for the extraction of parameters pertinent to defining how each fracture relates to one another. The utility of fracture wavefield events for the detection and characterization of fracture networks is evident in two cases: velocity anisotropy and wavefield reverberation.

Seismic Velocity Anisotropy

Compressional wave velocity anisotropy is a well documented phenomenon in which aligned inclusions cause seismic wave velocity to slow preferentially in the direction perpendicular to inclusion alignment (Backus, 1962; Hudson, 1981; Thomsen, 1995). As the leading pulse of seismic energy, or wavefront, passes through each fracture, it is slowed by the lower velocity fluid filling the fracture (Figure 2.4, right). The time the wave takes to traverse subsurface distances increases, and, therefore, observed velocity decreases, as a harmonic average of the distance occupied by each low velocity fracture fill zone and the distance occupied by each matrix velocity zone:

$$t_{perp} = \frac{\sum D_f}{V_f} + \frac{\sum D_m}{V_m} \tag{2.3}$$

where t_{perp} is the propagation time perpendicular to fracture strike, V_f is the velocity of the fracture fill, V_m is the velocity of the matrix material, D_f is the width occupied by each fracture, and D_m is the width occupied by the matrix material. If inclusions are aligned vertically, the anisotropy is called horizontal transverse isotropy to describe the horizontal axis of symmetry within the system. Fractures are most likely to produce this type of anisotropy due to the relative ease of opening a void space perpendicular to the downward direction of maximum stress in the subsurface.

The velocity of the seismic wavefield parallel to fracture alignment is unchanged by the presence of the slower velocity inclusions:

$$t_{parallel} = \frac{D_m}{V_m} \tag{2.4}$$

Velocity in this direction has not been visibly modified because the portion of the wavefront recorded has traveled through the faster matrix material only. This phenomenon is evident when related back to the seismic response of an irregular fracture interface (Figure 2.3, right). A wave traveling parallel to fracture alignment is incident upon only the tip of the fracture. Therefore, the portion of the wavefield that is directly in line with individual fracture locations will be diffracted or slightly transmitted through the long axis of the fracture. The resulting low-energy transmitted wave will be drastically slowed due to the time spent traversing the interior of the fracture, making it unlikely that this portion of the wavefield will be recorded. Therefore, from measurements of the direction and degree of compressional velocity anisotropy, the orientation of a fracture network (Hudson, 1981) and its relative fracture density (Grechka and Tsvankin, 1998; Thomsen, 2002) can be determined.

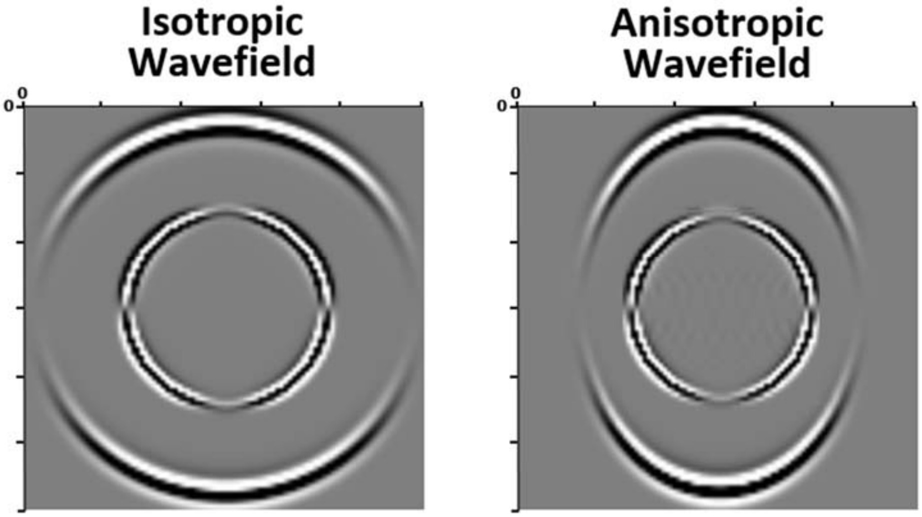

Figure 2.4: The effects of aligned fractures on compressional seismic velocity. As a seismic wave propagates out from the center of the model, an isotropic medium does not alter the wavefield velocity in any particular direction, and the compressional wavefront is shaped like a circle (left). A medium with high fracture density slows compressional wavefield velocity in the direction perpendicular to fracture strike but has no effect on wavefield velocity parallel to fracture strike. This distortion of the wavefront is known as anisotropy and results in a wavefront that resembles an ellipse (right). Note that the shear seismic wavefronts in both figures are unaffected by the presence of the gas filled fractures and maintain a circular shape.

Seismic Diffraction Coda

Wavefield reverberations are a less well-understood topic of study for fracture detection and characterization. A seismic wavefield traveling through a vertically fractured medium consists primarily of reflected waves that reverberate between the fractures (Figure 2.3, right). If fracture length is comparable to the seismic wavelength, these reverberations, or seismic coda (Aki and Chouet, 1975), will be coherent diffractions from individual fractures (Figure 2.5, left). The spacing of the seismic coda is proportional to fracture spacing (Figure 2.5, center) and decreases as the fracture spacing decreases (Schultz and Toksoz, 1996; Daley et al., 2002; Nakagawa et al., 2003; Chichinina et al. 2006). This relationship holds until the spacing between the fractures becomes less than the seismic resolution, or one fourth of the wavelength, and interference between the different coda signals causes cancellation and blurring of their shapes (Figure 2.5, right). Because the coda have reflected off of the fracture interface, they carry information about the impedance contrast at this boundary (Willis et al., 2004).

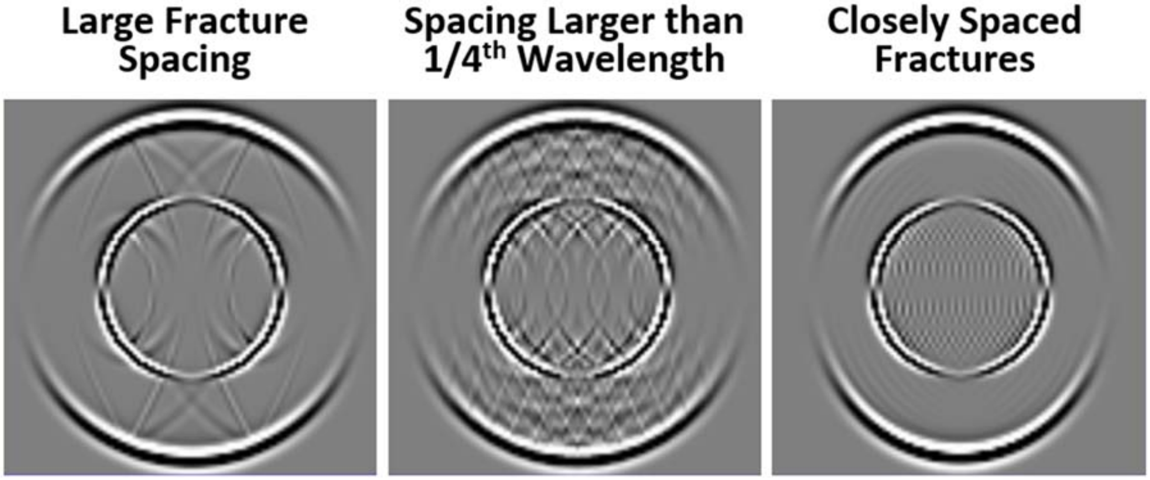
Large Fracture Spacing

Spacing Larger than 1/4th Wavelength

Closely Spaced Fractures

Figure 2.5: The effects of aligned fractures on compressional seismic wavefields in 2D. As a seismic wave propagates out from the center of a model, a medium with large fracture spacing, as in the left image containing two fractures, produces coherent diffractions, or seismic coda off the source-facing side of the fracture. A medium with fracture spacing that is larger than seismic resolution, or 1/4 of the wavelength as seen in the center image, will contain one distinct compressional and shear seismic coda for each fracture present in the medium. The spacing of the coda is proportional to fracture spacing and the strength of the coda is proportional to the velocity of the individual fracture's infill. When fractures are closely spaced, seismic coda undergo interference and cancellation, as seen in the right image.

As with compressional velocity anisotropy, seismic coda signatures are directionally dependent. The phenomena depicted in Figure 2.5 occur only in the direction perpendicular to fracture network strike (Schultz and Toksoz, 1996). In the same way that aligned inclusions slow seismic velocity in the direction perpendicular to inclusion alignment, the chaotic coda signature within the wavefield only occurs as a result of the wavefield interacting with and propagating through each fracture (Figure 2.6, left). The wavefield propagating parallel to fracture strike consists, instead, of parallel reflections from the elongated side of each fracture (Burns et al., 2007), and appear to represent a medium containing thin isotropic layers (Figure 2.6, right). However, wavefield variations parallel and perpendicular to fractures can only be documented when different azimuths are compared in 3D models. Therefore, seismic coda can provide information about fracture spacing within a network in 2D models, the direction of fracture strike in 3D models, and information about individual fracture infill if enough information is known about the surrounding matrix material.

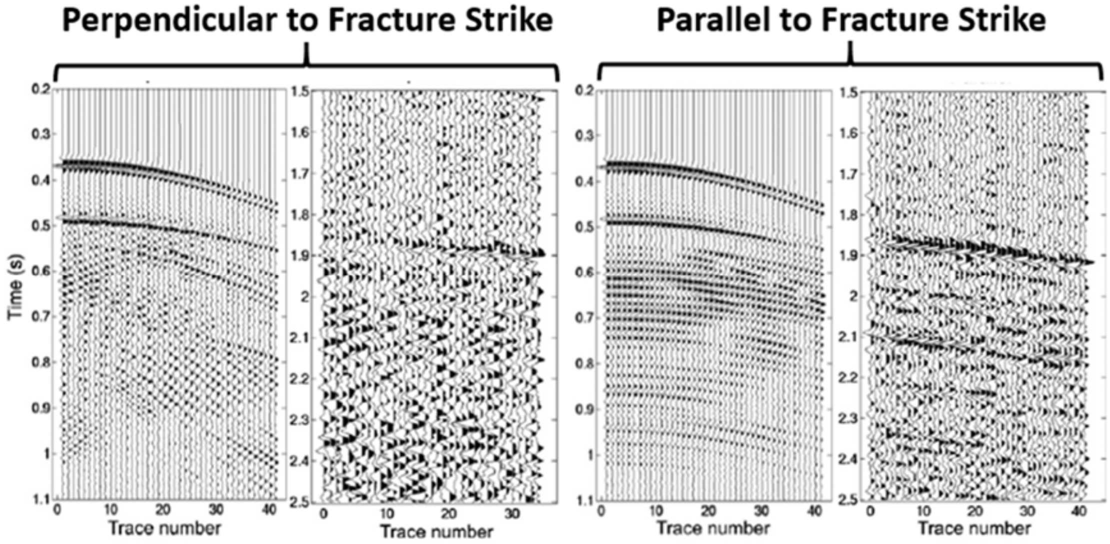

Figure 2.6: (Modified from Burns et al., 2007) The effects of aligned fractures on compressional seismic wavefields in 3D. Burns et al., (2007) modeled the seismic response to evenly spaced, parallel, 10 meter-wide, vertical, gas-filled fractures in 3D and compared the results to seismic data from the Emilio Field, a fractured carbonate. The images from left to right are as follows: Burns et al.'s modeled seismogram perpendicular to fracture strike, Emilio Field seismogram perpendicular to fracture strike, Burns et al.'s modeled seismogram parallel to fracture strike, and Emilio Field seismogram parallel to fracture strike.

SUMMARY

This chapter provides a background summary of pertinent phenomena encompassed in the topics of reflection, diffraction, and transmission that are required to understand the seismic response of an individual subsurface fracture. The irregular interface of a fracture differs from the textbook example of a layered interface in two significant ways: (1) fractures are narrow, elongate features with large curvature changes at each end and (2) fractures are normally associated with a strong decrease in impedance due to low density and velocity fluid infill. Snell’s Law illustrates the complex wavefield geometry resulting from aligned vertical fractures and Zoeppritz Equations illustrate the difficulty of reflecting and transmitting seismic energy through aligned fractures. Scattering attenuation is defined as the cumulative result of both the phenomena described in Snell’s Law and Zoeppritz Equations. Through the study of seismic velocity anisotropy and seismic coda properties, scattering attenuation can be used to estimate the orientation, geometry, and infill of fracture networks.

Chapter 3: Fundamentals of Discrete Fracture Modeling

REPRESENTATION OF A FRACTURE

When a seismic wave propagates through an anisotropic subsurface formation, the medium imparts a directional dependence on the propagation. This directional dependence can be caused by a variety of factors including alignment of platy mineralogy, variations in porosity, or the presence of fractures. Over the last thirty years, various equivalent medium theories have been developed that allow for the characterization of the mechanism causing formation anisotropy using seismic data. The findings of theories focused on fracture-related anisotropy are detailed in Chapter 2, which discussed directional variations in compressional velocity and seismic coda properties. Understanding the detailed relationship between a seismic wavefield and a fracture network is of little help to our interpretation if the theory used to model these interactions cannot realistically represent true fracture attributes. With this point in mind, finite element discrete fracture modeling techniques were chosen for this work to represent a fractured medium and to numerically propagate a seismic wave through that medium. This chapter demonstrates how discrete fracture finite element methods offer better control on modeling accuracy and more geometrical flexibility than other methods traditionally used.

Seismic Velocity in Fractured Rock

Before delving into the theories for numerically representing fractured media, the basic mathematics of how the presence of fractures affects seismic wave propagation must be discussed. Wave propagation is governed by the equation of motion:

$$\rho \frac{\partial^2 u_i}{\partial t^2} = \frac{\partial \sigma_{ij}}{\partial x_j} + \frac{\partial m_{ij}}{\partial x_j} + f_i \qquad i, j = 1, \dots, d \tag{3.1}$$

where d is the number of dimensions, ρ is the medium density, σ_{ij} is the stress tensor, m_{ij} is the moment tensor of the source, f_i is the source force vector, u_i is the displacement vector, and therefore $\partial^2 u_i/\partial t^2$ is the propagation acceleration (Sheriff and Geldart, 1995). Disregarding the source terms, it is apparent that the velocity at which a wave propagates through a medium is governed by the density of the medium and its ability to handle stress variations.

In an elastic medium, Hooke's Law shows that the stress tensor is linearly proportional to strain by implementation of the elastic stiffness tensor, C_{ijkl}:

$$\boldsymbol{\sigma_{ij}(u) = \ C_{ijkl}\,\varepsilon_{kl}(u)} \tag{3.2}$$

with

$$\boldsymbol{\varepsilon_{kl}(u) = \frac{1}{2}(\frac{\partial u_k}{\partial x_l} + \frac{\partial u_l}{\partial x_k})} \tag{3.3}$$

where ε_{kl} is the strain tensor. The stiffness of a rock is defined as the extent to which it resists deformation (Mavko et al., 2009). Factors that decrease the stiffness of a rock are an increase in the open space between grains or a decrease in the stiffness of the grains themselves, both of which allow the rock to compress when a force is applied. The relationship between the stiffness tensor and these tangible rock properties is revealed upon expanding equation 3.2 and using Voight notation to reduce C_{ijkl} to a 6 by 6 matrix:

$$\begin{pmatrix} \sigma_1 \\ \sigma_2 \\ \sigma_3 \\ \sigma_4 \\ \sigma_5 \\ \sigma_6 \end{pmatrix} = \begin{pmatrix} c_{11} & c_{12} & c_{13} & c_{14} & c_{15} & c_{16} \\ c_{12} & c_{22} & c_{23} & c_{24} & c_{25} & c_{26} \\ c_{13} & c_{23} & c_{33} & c_{34} & c_{35} & c_{36} \\ c_{14} & c_{24} & c_{34} & c_{44} & c_{45} & c_{46} \\ c_{15} & c_{25} & c_{35} & c_{45} & c_{55} & c_{56} \\ c_{16} & c_{26} & c_{36} & c_{46} & c_{56} & c_{66} \end{pmatrix} \begin{pmatrix} \varepsilon_1 \\ \varepsilon_2 \\ \varepsilon_3 \\ \varepsilon_4 \\ \varepsilon_5 \\ \varepsilon_6 \end{pmatrix} \tag{3.4}$$

Symmetry reduces C_{ij} to only two independent constants in an isotropic medium:

$$\begin{bmatrix} c_{11} & c_{12} & c_{12} & 0 & 0 & 0 \\ c_{12} & c_{11} & c_{12} & 0 & 0 & 0 \\ c_{12} & c_{12} & c_{11} & 0 & 0 & 0 \\ 0 & 0 & 0 & c_{44} & 0 & 0 \\ 0 & 0 & 0 & 0 & c_{44} & 0 \\ 0 & 0 & 0 & 0 & 0 & c_{44} \end{bmatrix} c_{12} = c_{11} - 2c_{44} \tag{3.5}$$

This simplification to Hooke's Law allows the stiffness components to be defined in terms of Lame's Parameters:

$$c_{11} = \lambda + 2\mu, \quad c_{12} = \lambda, \quad c_{44} = \mu \tag{3.6}$$

where μ is called the rigidity, or shear modulus and λ is called the fluid incompressibility modulus.

It can be shown further that velocity is directly related to Lame's Parameters:

$$V_{\mathrm{P}} = \sqrt{\frac{c_{11}}{\rho}} \qquad V_{\mathrm{S}} = \sqrt{\frac{c_{44}}{\rho}} \tag{3.7}$$

where ρ is rock density and V_p and V_s are compressional and shear velocity, respectively (Mavko et al., 2009). It is clear from equation 3.7 that the propagation velocity of seismic waves is directly proportional to the rigidity of a rock and the incompressibility of the fluid contained within the rock. More compliant regions slow velocity simply because the compressional movement of the material dampens wave propagation. Therefore, within a uniform rock matrix, the presence of open or fluid-filled fractures act to decrease the total stiffness by closing or giving way slightly as a seismic wave propagates past them.

Discrete Fracture Models versus Effective Medium Models

Of the many types of equivalent medium theories that exist, the two most commonly applied in seismic-based fracture research are effective medium models and discrete fracture models. Effective medium models describe the macroscopic elastic properties of a composite material by averaging the elastic properties of the constituent materials (Figure 3.1, left). To quantify the increase in matrix compliance caused by fluid-filled fractures, effective medium models simply subtract stiffness from the composite layer and, therefore, decrease velocity within the layer. The new effective elastic stiffness tensor is a function of three terms:

$$C_{ij}^{eff} = C_{ij}^{0} - C_{ij}^{1} - C_{ij}^{2} \tag{3.8}$$

$$\text{with} \quad C_{ij}^{1}, C_{ij}^{2} = f(\lambda, \mu, \kappa, \alpha, \varepsilon)$$

The first term represents an isotropic background, defined by Lame's Parameters in equation 3.6, and the second two corrections represent stiffness subtracted from the system due to the presence of a single fracture set. The correction terms are defined by estimations of average values of Lame's Parameters (λ, μ), bulk modulus (κ), fracture density (ε) and fracture aspect ratio (α) for the fractured layer (Hudson 1980, 1981; Cheng, 1993; Mavko et al., 2009).

Discrete fracture models differ from effective medium models in that the former retains individual fracture attributes in space instead of averaging these attributes into one set of stiffness parameters for each fractured layer present in the system (e.g. Schoenberg, 1980, 1988; Coates and Schoenberg, 1995; Zhang, 2005; Vlastos, 2005; Willis et al. 2004, 2006; Grandi-Karam, 2008). In discrete fracture finite element models, a gridded mesh represents the fracture attributes in space, and each grid cell can either represent a location of isotropic background or fracture interior with associated fill (Figure 3.1, right). The interface between background matrix cells and fracture cells is modeled as a linear slip surface, which defines a linear relationship between the traction along the fracture surface, τ_j, and the jump in displacement, $[u_i]$, across the fracture within the matrix material (Sayers and Kachanov, 1991):

$$[u_i] = S_{ij}\tau_j \tag{3.9}$$

with $S_{ij} = C_{ij}^{-1}$

Because each fracture remains as an individual physical entity rather than as part of the stiffness tensor, wavefield scattering and attenuation patterns resulting from fracture interfaces can be studied in a more practical manner. Therefore, discrete fracture finite element modeling methods were chosen for this study to best accomplish the objective of understanding the seismic response to realistic subsurface fracture.

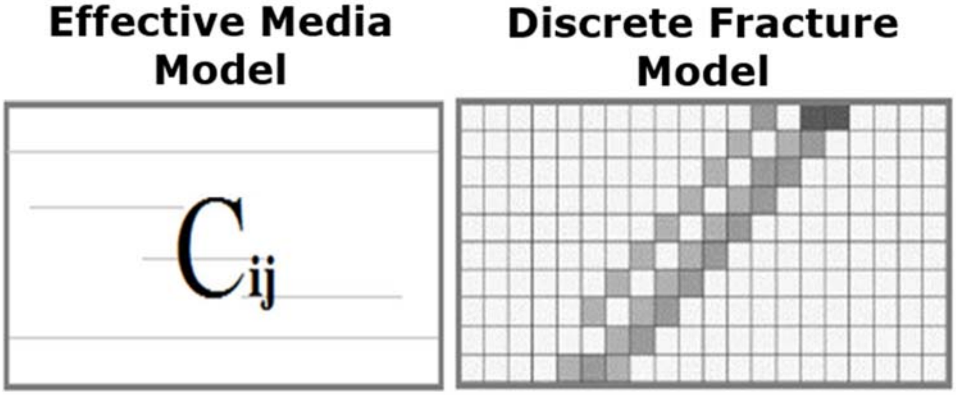

Figure 3.1: (Modified from Oliver et al., 2012) Different representations of fractured media. An effective medium model averages the attributes of a fracture set within a specific layer to compute the effective stiffness tensor Cij that defines the wave propagation velocity through the medium (left). The discrete fracture finite element model discretizes the medium into grids that allow each individual fracture to be defined at a specific location within the medium (right). In this image, lighter grids represent an isotropic background, and darker grids represent fracture interior. Normal and tangential compliance are computed along the fracture-matrix interface to define wave propagation velocity through the medium.

Fractures as Linear Slip Surfaces

Discrete fracture models represent fractures as linear slip surfaces within a modeled mesh by utilizing the elastic compliance tensor, S_{ij} in equation 3.9, instead of its inverse, stiffness. In this scheme, compliance from the presence of open or fluid-filled fractures is added to the system by summing the displacement discontinuities along every plane of weakness, or slip surface, at the fracture-matrix interface (Sayers and Kachanov, 1991; Zhang et al., 2009):

$$S_{ijkl} = S^0_{ijkl} + \sum_{r=1}^{N} S^r_{ijkl} \tag{3.10}$$

with $S^r_{ijkl} = f(\beta^r_N, \beta^r_T, n^r_i A^r)$

The first term again represents an isotropic background, as in effective media theory, but the second correction term systematically sums the effect of each fracture, r, from the first to the Nth. The compliance of each fracture, S^r_{ijkl}, is defined by the displacement discontinuity normal to the fracture face (β^r_N), the displacement discontinuity tangential to the fracture face (β^r_T), ith component of the normal to the rth face (n^r_i), and the area of the fracture plane (A^r).

Furthermore, the displacement discontinuities normal and tangential to the fracture face, called normal and tangential compliance, respectively, are defined as follows:

$$\beta_N = r^w \frac{4\mu}{\pi\alpha}\left(1 - \frac{\beta^2}{\alpha^2}\right)\left(1 + \frac{2\sqrt{r^w}}{\sqrt{\pi}}\right) + \frac{\kappa' + 4/3\,\mu'}{\Delta} \tag{3.11}$$

$$\beta_T = r^w \frac{8\mu(1 - \beta^2/\alpha^2)}{\pi\alpha(3 - 2(\beta^2/\alpha^2)}\left(1 + \frac{2\sqrt{r^w}}{\sqrt{\pi}}\right) + \frac{\mu'}{\Delta} \tag{3.12}$$

where α, β, and μ are the P-wave velocity, S-wave velocity, and rigidity of the rock, and r^w is the proportion of the fracture surface area that consists of welded contact, a is the mean radius of the contact areas, μ' and κ' are the rigidity and bulk modulus of the fracture fill, and Δ is the mean aperture of the fracture (Hudson et al., 1997; Worthington and Lubbe, 2007). These two variables, normal and tangential compliance, act as input parameters for fracture modeling using SWP3D, and the values used to compute them will be discussed in Chapter 4. Each modeled fracture can be defined individually in this way.

For this study, all fractures within a specific model are defined using a single normal and tangential compliance for the set. Importantly, discrete fracture models, with all their unknowns, are only as realistic as their input parameters. Without a good understanding of what discrete fracture parameters should be, the simplification, homogenization, and predictive capability of effective medium models gives the latter the advantage.

NUMERICAL ELASTIC WAVE PROPAGATION

To simulate wave propagation through a gridded mesh, either the acoustic wave equation, which only models compressional waves, or the elastic wave equation, which models both compressional and shear waves, must be computed at a discrete number of points along the propagation path. The ability to model both types of seismic waves generated in the subsurface allows the elastic wave equation to more realistically and more accurately represent the seismic response to subsurface features. Therefore, the elastic wave equation was chosen for this study. For a quick derivation of the elastic wave equation, the strain equation (3.3) and isotropic stiffness parameters (3.6) can be substituted into the generalized version of Hooke's Law in equation 3.2 to define stress in terms of the Lame's Parameters and strain:

$$\sigma_{ij}(u) = \lambda\delta_{ij}\varepsilon_{kk} + 2\mu\varepsilon_{ij} \tag{3.13}$$

where again σ_{ij} is the stress tensor, ε_{ij} is the strain tensor, λ and μ are Lame's Parameters, and δ_{ij} is the Kronecker Delta. Substituting this isotropic version of Hooke's Law into the equation of motion (3.1) yields the elastic wave equation (Sheriff and Geldart, 1995):

$$\rho\frac{\partial^2 u_i}{\partial t^2} - \lambda\frac{\partial}{\partial x_i}(\frac{\partial u_j}{\partial x_j}) - \mu\frac{\partial}{\partial x_j}(\frac{\partial u_i}{\partial x_j} + \frac{\partial u_j}{\partial x_i}) = \frac{\partial m_{ij}}{\partial x_j} + f_i \tag{3.14}$$

By choosing the elastic rather than the acoustic case, the mathematics of wave propagation becomes complicated by the need to solve the partial differential equation in (3.14). The analytic solution to a partial differential equation is difficult or impossible to obtain when it is computed on an irregular or unsmooth mesh, as is the case with media containing discontinuous fracture interfaces (Johnson, 1990).

The Finite Element Method for Wave Propagation

To circumvent the issues of modeling the elastic wave partial differential equation, elements of the surrounding model mesh are used to help smooth the solution at a discontinuous location (Figure 3.2). Common techniques, such as the finite difference method, approximate the partial derivatives of the wave equation using simple Taylor series expansion (Marfurt, 1984). The finite element method, by contrast, utilizes a manipulated form of the wave equation to weaken its differentiability requirements allowing for discontinuities in the medium. The elastic wave equation (3.14) is rewritten using Einstein's summation notation for ease of view:

$$\rho\partial_{tt}u_i - \partial_i\lambda\partial_j u_j - \partial_j\mu(\partial_j u_i + \partial_i u_j) = f_i \quad \text{in} \quad \Omega \tag{3.15}$$

where $\Omega \subset R^d$ is the physical domain, d is the number of dimensions, and the shorthand notation $\partial_l \partial u_k = \partial u_k/\partial x_l$ is used. Multiplying this so-called strong formulation of the elastic wave equation by a vector test function gives:

$$\int_\Omega \left(\rho\partial_{tt}u_i - \partial_i\lambda\partial_j u_j - \partial_j\mu(\partial_j u_i + \partial_i u_j)\right)v_i \, d\Omega = \int_\Omega f_i v_i \, d\Omega \tag{3.16}$$

where v_i is the test function assumed to be smooth in the domain (De Basabe and Sen, 2009). As a final step, integration by parts with the Gauss divergence theorem is performed on the second and third terms on the left side of equation 3.15, which results in the weak formulation of the elastic wave equation:

$$\begin{aligned}&\partial_{tt}\int_{\Omega}\rho u_i v_i \, d\Omega+\int_{\Omega}\left(\lambda\partial_i u_i \partial_j v_j+\mu(\partial_j u_i+\partial_i u_j)\partial_j v_i\right)d\Omega\\&-\int_{\Gamma}\left(\lambda\partial_k u_k n_i+\mu(\partial_j u_i+\partial_i u_j)n_j\right)v_i \, d\Gamma=\int_{\Omega} f_i v_i \, d\Omega\end{aligned} \tag{3.17}$$

where Γ is the boundary of Ω and n_i is a vector outward normal to Γ (De Basabe and Sen, 2009).

The above equation is called weak because the solution only contains first-order spatial derivatives (De Basabe, 2009; Oliver, 2012). This method for solving the partial differential equation is preferred over other methods, such as the finite difference method, because the solution can be represented as a system of linear equations instead of simply replacing the derivatives with approximations (Suli and Mayers, 2006). This method is also preferred for modeling fractures, whose interiors represent a discontinuity in space. The finite element method does, however, require at least nine adjacent nodes within the mesh to accurately calculate the two dimensional wavefield at a single location (Marfurt, 1984). Each of the nine nodes must also have both horizontal and vertical degrees of freedom in order to model the elastic vector quantities in the wave equation, which is more computationally intensive than other methods (Figure 3.2, right).

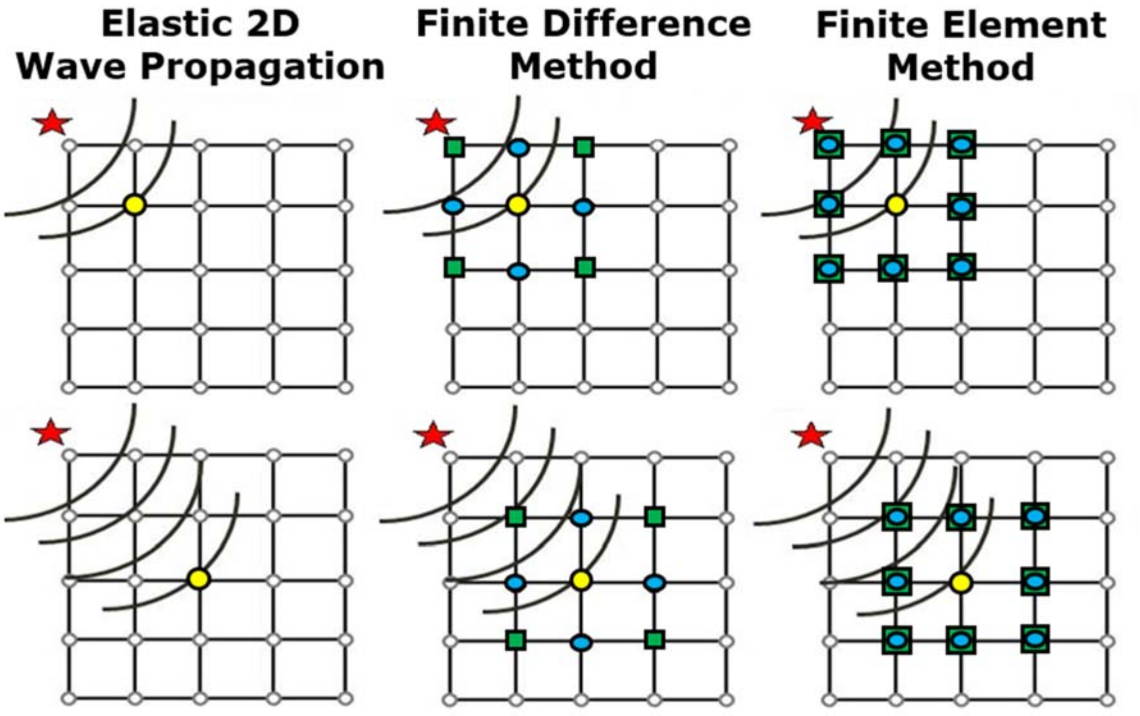

Figure 3.2: Diagram of the finite element method for numerical wave propagation through a discontinuous medium. A seismic source, represented by the red star in the top left corner of each frame, produces a wavefront whose propagation is represented by the black arcs (left). As the wavefront advances, the wavefield must be recalculated at each grid node it encounters, indicated in yellow. At discontinuous points where the exact solution does not exist, finite element methods utilize neighboring nodes surrounding the problem node to smooth the solution at this particular location (right). In 2D elastic wave propagation, a minimum of nine adjacent nodes are required to maintain a smooth solution throughout the medium and each of the nine nodes must have both horizontal degrees of freedom, represented by the blue dots, and vertical degrees of freedom, represented by the green boxes. To better illustrate this point, the finite difference method is shown in the center, which only requires four surrounding nodes to have vertical or horizontal degrees of freedom.

Interior-Penalty Discontinuous Galerkin Method

Although the finite element weak formulation of the elastic wave equation is advanced in its ability to obtain smooth solutions on irregular or fractured meshes, it was rarely implemented until the last 10 years. The reason lies in its reliance on linear systems that have the costly drawback of requiring inversions of large matrices to arrive at a solution (Johnson, 1990). The slowness of this inversion process and the computational power needed to perform such calculations greatly limited the use of finite element methods until recent advancements in computer power and wave propagation theory were made. In this study, the Interior-Penalty Discontinuous Galerkin method (IP-DGM) is used to avoid the inversion process by weakening the wave equation further. To do so, the domain Ω is divided into nonoverlapping elements, E_i, that cover the entire domain such that $\Omega_h = \{E_i;\ \ i = 1, \ldots, N\}$ (De Basabe and Sen, 2009). The wavefield is allowed to be discontinuous at the edges of these elements, so instead of attempting to integrate by parts over the entire domain, integration is performed within the interior of the elements and then added together (De Basabe, 2009):

$$\sum_{E\in\Omega_h} \left(\left(\rho\partial_{tt}\mathbf{u}, \mathbf{v} \right)_E + B_E(\mathbf{u}, \mathbf{v}) \right) + \sum_{\gamma\in\Gamma_h} J_\gamma(\mathbf{u}, \mathbf{v}; s, \sigma) = \sum_{E\in\Omega_h} (\mathbf{f}, \mathbf{v})_E \tag{3.16}$$

The above equation has been weakened further to only contain first-order space and time derivatives and, therefore, allows for discontinuities in both the medium and the wavefield (Grote et al., 2006). Therefore, IP-DGM speeds computation and better accommodates discontinuities in the wavefield created by fluid-solid and free-surface boundary conditions present at fracture interfaces (De Basabe, 2009; De Basabe et al., 2011). From the literature outlined above, clearly finite element methods are the best option for accurately modeling the seismic response of fractures. The same qualities that make FEM so attractive are also the reasons why it has been rarely used for geophysical applications in the past. The construction of such a robust numerical wave propagation model requires a very skilled programmer and a substantial amount of time. Fortunately, in this study, I implement an open source development code outlined in De Basabe (2009) to circumvent this drawback.

SUMMARY

This chapter provides a background summary of the theory behind modeling discrete fractures within a host matrix material and numerically propagating a seismic wave through that material. The velocity at which a seismic wave propagates through a medium is directly proportional to the elastic stiffness of that medium. The presence of open or fluid-filled inclusions within that medium act to decrease the total stiffness by partially closing as the seismic wave propagates past them. The discrete fracture finite element modeling method used in this study adds compliance to each fractured region by relating the fracture-host material interface, or discontinuity, to the traction along that interface. The Interior-Penalty Discontinuous Galerkin Finite Element numerical wave propagation method also specifically focuses on the discontinuity present at the fracture interface when solving the elastic wave partial differential equation. The wave equation is weakened, in short, by dividing the modeled domain into smaller elements that are bounded by the discontinuities. By calculating the wavefield in each element and summing the results, computationally prohibitive mathematics are avoided, and the medium and wavefield are allowed to contain discontinuous voids or jumps that are naturally present when fractures are present.

Chapter 4: Methodology of Modeling Individual Fracture Attributes

INTRODUCTION

In order for a synthetic seismic study to have useful results, it must realistically model the feature of interest and accurately calculate the seismic response to that feature. Although this study uses the most realistic discrete representation of a fracture and the most accurate element by element calculation of a discontinuous wavefield, Chapter 3 showed the vast number of variables that make up all of the associated equations. Therefore, the principal component to obtaining useful results from synthetic seismic studies is to thoughtfully choose or understand the implications of using default values for each variable implemented. Seismic Wave Propagation 3D (SWP3D) is an open source software to create model meshes and to numerically propagate a wave through the model. De Basabe (2009) developed and thoroughly tested the code and comprehensively discussed recommended parameters for best modeling results. To run this program, an input file is used that is divided into three main categories: wave propagation parameters, model background parameters, and a special section for fracture parameters. The following sections discuss the values chosen for the pertinent variables defined in a general input file used in this study.

MODEL CONSTRUCTION WITH SWP3D

Defining Wave Propagation Parameters

As mentioned in the previous chapters, this study models the elastic wave equation in two dimensions, X and Z. In order to model fractures, however, physical model type must be chosen as “FRAC”, which is also elastic. Though two other numerical modeling methods are available in SWP3D, I have chosen to use the Finite Element Discontinuous Galerkin method because it is the most robust technique for modeling fractured media, as argued in chapter 3. Per the recommendations for best results with this technique outlined in De Basabe (2009), Finite Element order was chosen to be 5th, Discontinuous Galerkin type was chosen to be Symmetric Interior Penalty Galerkin (SIPG) with a penalty of 4 and a mass lumping of 1, basis shape function type was chosen to be Nodal Gauss-Lobatto-Legendre (Nodal-GLL), and no penalty is placed on propagation velocity. The time stepping method is simple 2nd order Finite Difference (FD), and the stability condition for time stepping (CFL) was chosen to be 0.02 from personal correspondence with Dr. De Basabe.

Defining Background Parameters

Source Parameters

To best mimic conventional seismic surveying techniques, the seismic source is centered at the top of the model along with 298 receivers spaced 10 meters apart that span the total modeled horizontal distance (Figure 4.1, top-left). The source was chosen to be a point source that produces a 23 Hz pulse downward in the positive z-direction. In an isotropic model, only the P-wave and S-wave should be generated and propagate into the model. When checked, however, a linear feature was noticed propagating off of the apex of the S-wave out toward the tail of the P-wave (Figure 4.1, top-right). Though this feature appeared to be a head wave, an isotropic model contains no interface for the S-wave to interact with to form a head wave.

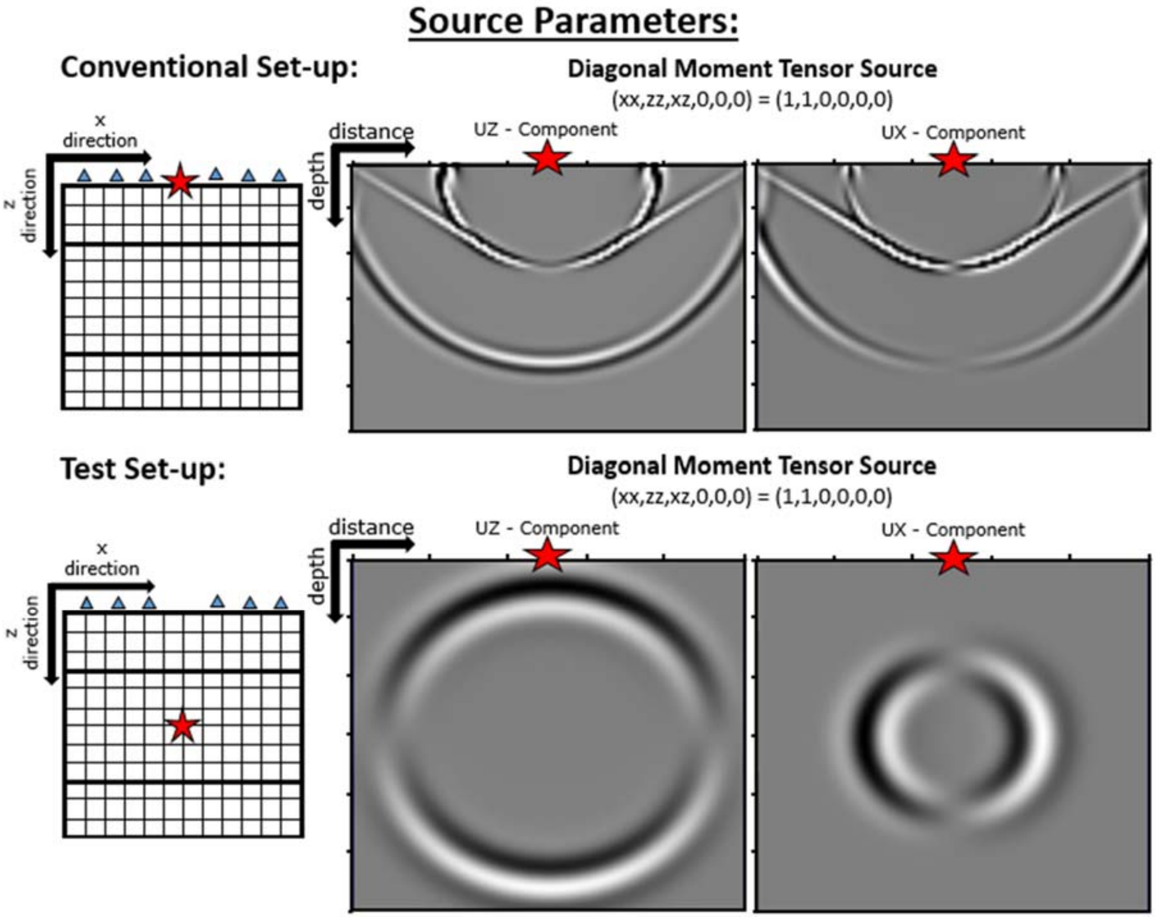

Figure 4.1: Comparison of the two components of wave motion to determine the origin of the linear features connecting the P-wave and S-wave. The first row shows a conventional scenario for seismic surveying in which the source, red star, and receivers, blue stars, are aligned at the top of the model (left) and the wave propagates down into the model (right). The second row shows a test model with receivers aligned along the top of the model and the source in the center of the model so that the wave propagates out in all directions. With a diagonal source, only shear movement should be felt by the receivers in the Ux direction and only compressional movement should be felt by the receivers in the Uz direction. Because this is not the case when the source is at the top of the model, it can be deduced that linear features are head waves from the source's interaction with the upper-most model boundary.

As a test, the source was changed from z-directed downward pulse to a diagonally directed pulse. With this type of source, only shear movement should be recorded as the x-component of motion by the receivers and only compressional movement should be recorded as the z-component of motion by the receivers. When the diagonal source was placed at the top of the model, the wavefield appeared only slightly different than the strictly z-directed source, which is counterintuitive. When the diagonal source was placed in the center of the model, however, the wavefield appeared as expected, with only slower S-wave motion recorded as the x-component of motion and only faster P-wave motion recorded as the z-component of motion (Figure 4.1, bottom-right). The conclusion from this experimentation was that the linear feature propagating off of the S-wave was indeed a head wave caused by the interaction of the S-wave with the interface at the top of the model.

Absorbing Boundary Parameters

Without absorbing boundaries applied, a model becomes cluttered with reflections off of the model edges that are unnatural and cloud interpretation (Figure 4.2, top-left). Although SWP3D has four types of absorbing boundary conditions available, only the Tapering Boundary Condition has been implemented for use with the Discontinuous Galerkin method (De Basabe, personal correspondence). The tapering parameters alpha and beta define the onset of tapering and how severely the wavefield is truncated, respectively. To find the best tapering parameters for this study, models were generated with a range of alpha and beta values, the most pertinent of which are shown in Figure 4.2. When compared to the model with no defined absorbing boundaries in the top-left corner, it can be discerned that when beta is equal to zero, the largest amount of absorption at model boundaries occurs. Also apparent is that small values of alpha prevent the removal of expected P-wave polarity reversals upon reflecting off of the model boundary.

Therefore, the values deemed most effective and implemented in this study are alpha equal to 0.005 and beta equal to zero (Figure 4.2, bottom-left).

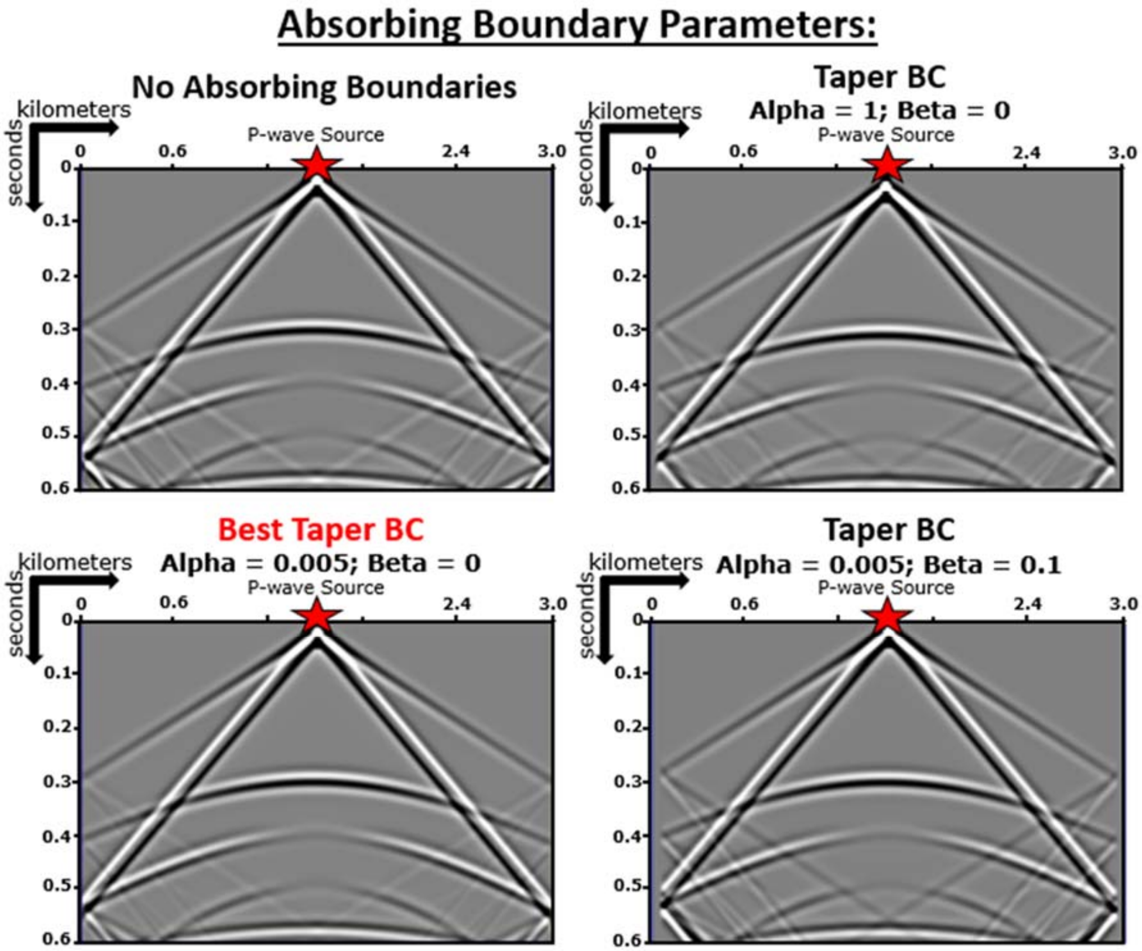

Figure 4.2: Comparison of various values of alpha and beta tapering parameters for the creation of tapering absorbing model boundary conditions. When compared to the model with no defined absorbing boundaries (top-left), it can be discerned that small values of beta have the largest effect on absorption at model boundaries and small values of alpha prevent the removal of P-wave polarity reversals upon reflecting off of the model boundary. The values deemed most effective and implemented in this study are bolded in red (bottom-left).

Mesh Parameters

In this section, the extent of the model and background matrix velocity and density are defined. For this study, the background material could easily be modeled as sandstone, shale, or limestone. The variability of velocity and density in shales makes modeling the generic seismic response to that material difficult, and it was removed from contention. Because limestone rocks have, on average, a noticeably higher velocity that sandstones, a wave in limestone (Figure 4.3, left) will propagate quickly through the model and reflect off of the boundaries more quickly than a wave in sandstone (Figure 4.3, right). Because seismograms are shown in time, both direct wave velocities will reach the model boundaries at the same apparent “depth”, though the wave through limestone will reach that apparent depth much more quickly than a wave in sandstone. Therefore, the faster wave on the left of Figure 4.3 will cover the shorter total distance traveled by the slower wave on the right in about one-third of the time. Thus, the background matrix was modeled as a limestone, with a P-wave velocity of 4,600 m/s, an S-wave velocity of 2,400 m/s, and a density of 2,400 kg/m^3, to decrease model computation time.

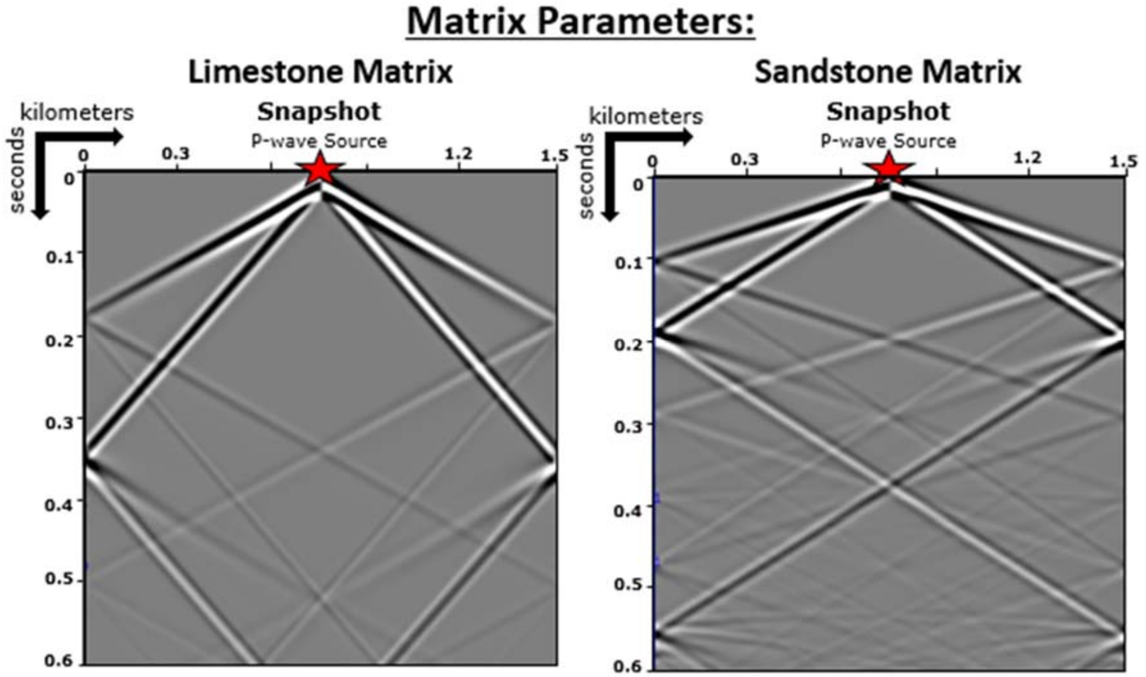

Figure 4.3: Comparison of the effect of matrix velocity on the resulting wavefield in a model with imperfectly absorbing boundary conditions. When velocity is large, as in a limestone (left), the wave propagates quickly through the model and reflects off of the boundaries more quickly than when velocity is small, as in a sandstone (right). Because seismograms are shown in time, both direct wave velocities will reach the model boundaries at the same apparent depth. Therefore, to cover only the shorter distance traveled by the slower wave on the right, the faster velocity model on the left will only have to be run about one-third of the time as the right model, which is optimal.

To minimize boundary reflections, the model shown in Figure 4.3, which is a 1.5 by 1.5 kilometer square, must be widened. The effect of this change is visually similar to the effect of velocity change. If the model becomes wider, velocity will appear to slow because the time it takes to propagate out to the boundaries has increased, and the wave is able to travel deeper within the model before boundary reflection occurs. A wider model will, therefore, act to optimize the area within the seismogram that is not contaminated by boundary reflections. Models in SWP3D must be square to be saved as readable binary files. Therefore, a balance between model width and total model run time had to be reached. The model width chosen was 3 by 3 kilometers, or double that shown in Figure 4.3.

A way around the constraint of modeling square meshes is the choice of model run time. Though the model used in this study extends down 3 kilometers, the total propagation time can be set so that it is only long enough to record specific reflections within the upper portion of the model. The optimal area for studying seismic wavefield variations to fracture parameters will be within the area of the seismogram that is not contaminated by boundary reflections. Thus, the only area within the model that should be recorded is within this uncontaminated zone, delineated in yellow on the left side of Figure 4.4. The time to the direct P-wave intersection point at the base is the one-way distance traveled by the P-wave, 3,000 meters, divided by P-wave velocity, 4,600 m/s, plus an extra 0.1 second for the source's time delay. Therefore, the optimal model run time is 0.752 seconds, even though this is only simulated wave propagation time and not the actual time the model takes to run.

To test the seismic response to various fracture attributes, fractures are systematically added to a horizontal layer within the model. Again, to optimize view of fracture-related wavefield features, the fractured interval must be centered within the uncontaminated zone in the polygon created by the direct P-wave. From model run time, it is calculated that the deepest features recorded lie at a depth of approximately 1,500 meters. Therefore the recorded portion of the model can be divided into three even subdomains, with the fractured subdomain extending from 500 to 1,000 meters depth (Figure 4.4, right).

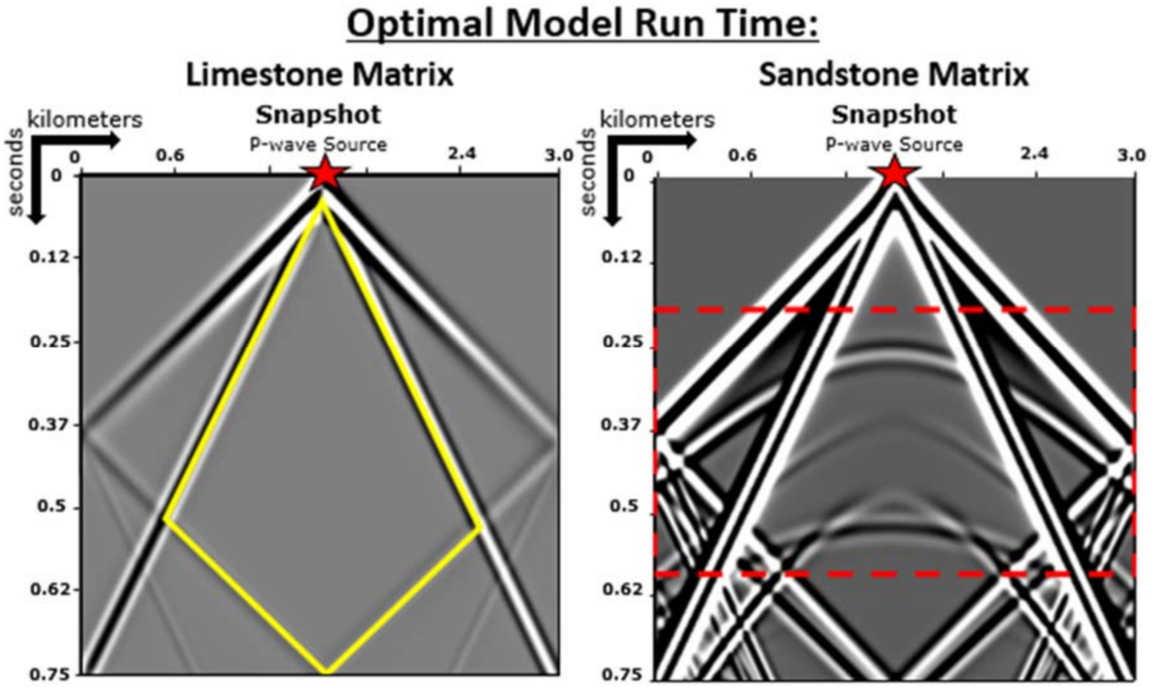

Figure 4.4: Illustration of fractured interval placement and determination of model run time. After optimal model width has been determined, the fractured interval, boxed in red on the right, is centered within the area of the seismogram that is less contaminated by boundary reflections, outlined in yellow on the left in the isotropic model. Because the model must be symmetric and because the fractured interval must be located shallowly for optimal placement within the seismogram, a large portion of the model is unnecessary. Therefore, wave propagation is cut short at 0.752 seconds to preserve only the fractured interval reflections and a buffer zone below.

Grid Parameters

After material properties are added to the mesh, it must be discretized into uniform grids upon which nodes are placed so that the wavefield can be calculated. Discretization presents another time optimization problem: as the number of grids is increased, the time the model takes to complete its calculations exponentially increases. An arbitrarily small number of grids cannot be chosen simply to speed up the real time in which the model runs because of a phenomenon called grid dispersion. Grid dispersion is solely the product of numerical calculation and does not exist in real seismic data. The Finite Element method is best at modeling fractured materials because it more thoroughly utilizes nodes of the surrounding mesh to smooth the wave equation solution at a discontinuous location (Figure 3.2 in chapter 3). This smoothing of the solution, however, creates signal where no signal should occur (Figure 4.5, right). When a mesh is sufficiently fine, enough nodes exist in each area so that discontinuities can be overcome without using and contaminating nodes located far away from the node in question.

To determine how fine a grid must be to prevent contamination of the wavefield with grid dispersion the following equation is used:

$$N = \frac{Vs/f}{x/\Delta x} > 5 \tag{4.1}$$

where Vs is the shear velocity, f is the source peak frequency, x is the distance along the x-axis, and Δx is the number of the grids in the x-direction (De Basabe, personal correspondence). In this case, shear wave velocity is 2,400 m/s, peak frequency of the source is 23 Hz, distance along the x-axis is 3,000 meters, and the grid size is 10 by 10 meters allowing for 300 grids along the x-axis (Figure 4.5, left). Therefore N = 10.4 and is well above the required value of 5. The grid in this study is excessively refined in this way to model "thin" fractures that are limited in width to the width of an individual grid cell and cannot be smaller.

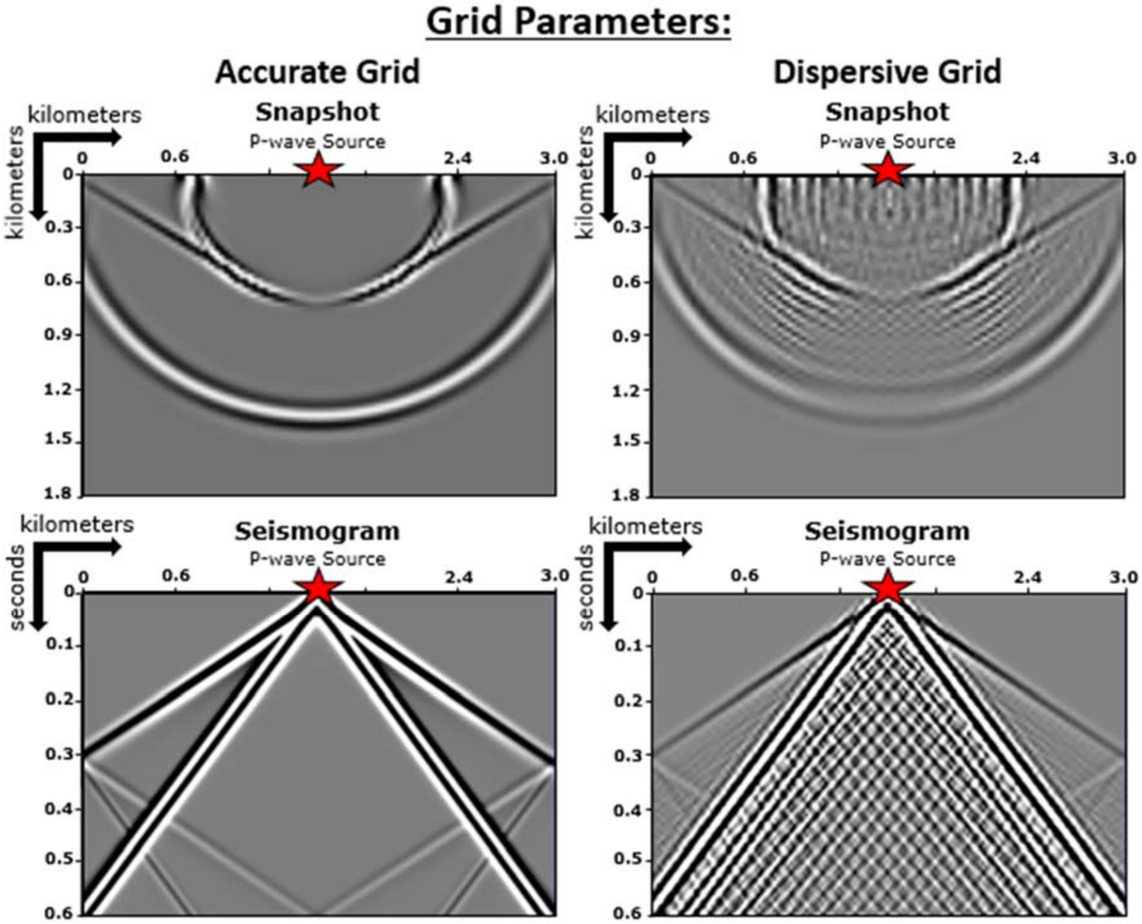

Figure 4.5: Comparison of differences in the ratio of length of the model in the x-direction to number of grids in the x-direction. When this ratio is small, i.e., grid width is small and the number of grids in the x-direction is large, grid dispersion is insignificant, and all energy contained within the model can be considered the result of wave interaction with the modeled mesh (left column). When this ratio is small, i.e. the grid width is large and the number of grids in the x-direction is small, grid dispersion is significant and generates energy within the model that is unrelated to features in the model mesh (right column).

Defining Fracture Parameters

The last section of the input file involves the addition of fractures to a model. Recall from chapter 3 that in discrete fracture finite difference gridded meshes, fractures are defined by the compliance they add to the matrix material by closing or giving way slightly as a seismic wave propagates past them. Therefore, fractures that are filled with easily compressible gas will add significantly more compliance to the matrix than less easily compressible oil or effectively incompressible water or cement. Recall also from chapter 3 that fracture compliance is divided into a component normal to the fracture face and a component parallel, or tangential, to the fracture face. This division is important in long slender features such as fractures because the ease of compressing the widest opening of the fracture in its center will be much greater than at its thin curved ends.

Using equations 3.11 and 3.12, the normal compliance and tangential compliance of a fracture can be calculated based on the P-wave velocity, S-wave velocity, and rigidity of the matrix material, the rigidity and bulk modulus, or incompressibility, of the fracture fill, the proportion of the fracture surface area that is a welded contact, the mean radius of the contact areas, and the mean aperture of the fracture. Recall from the section above that fracture width had to be set to the unrealistic value of 10 meters due to constraints on the time it would take to model with a finer grid. Therefore, to obtain more realistic values of compliance, fracture aperture was set to 1 meter in equations 3.11 and 3.12. The proportion of welded surface along the fracture was set to 0.15 to account for the welded ends of each fracture, and the contact radius was set to 0.5 or half of the fracture aperture. Table 4.1 lists the different velocities and bulk moduli, K, of the various materials used in this study and the resultant normal and tangential compliances utilized in the input file.

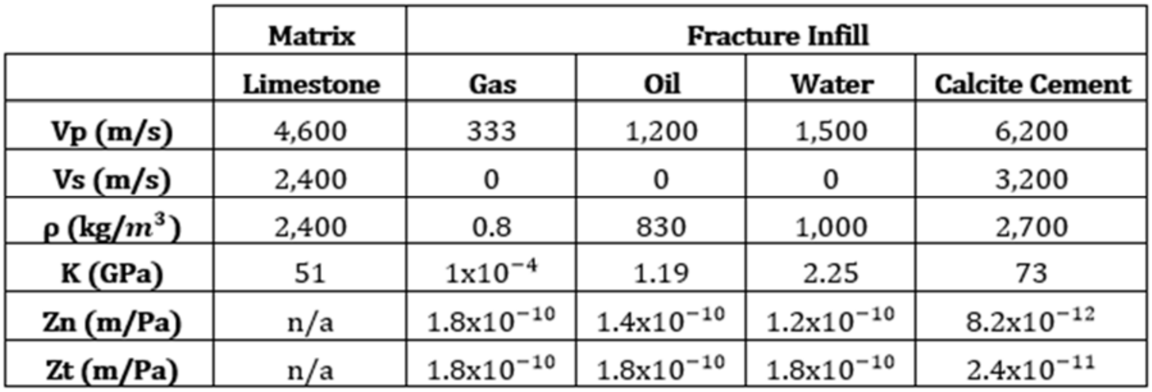

	Matrix	Fracture Infill			
	Limestone	Gas	Oil	Water	Calcite Cement
Vp (m/s)	4,600	333	1,200	1,500	6,200
Vs (m/s)	2,400	0	0	0	3,200
ρ (kg/m^3)	2,400	0.8	830	1,000	2,700
K (GPa)	51	$1x10^{-4}$	1.19	2.25	73
Zn (m/Pa)	n/a	$1.8x10^{-10}$	$1.4x10^{-10}$	$1.2x10^{-10}$	$8.2x10^{-12}$
Zt (m/Pa)	n/a	$1.8x10^{-10}$	$1.8x10^{-10}$	$1.8x10^{-10}$	$2.4x10^{-11}$

Table 4.1: Elastic parameters used to define each material modeled: compressional wave velocity (Vp), shear wave velocity (Vs), density (ρ), bulk modulus (K), normal compliance (Zn), and tangential compliance (Zt). These values were gathered from Bourbie et al. (1987) and Mavko et al. (2009).

PHASES OF FRACTURE NETWORK MODELING

The isotropic limestone model defined in the previous sections is divided into three separate subdomains, delineated by the bolded horizontal lines in Figure 4.6. Fracture modeling consists of populating the center subdomain with three phases of fracture attribute alteration. Phase 1 tests the seismic response to a single idealized vertically fractured cluster centered directly below the seismic source within the center subdomain (Figure 4.6, right). Fracture spacing was uniformly decreased between each fracture from 1000 meters, allowing for only 2 fractures in the cluster, to 10 meters, allowing for 150 fractures in the cluster. In this last scenario, fracture spacing is equal to fracture width and, therefore, represents a horizontal transversely isotropic medium. Next, the length of all fractures within the cluster is shortened from 500 meters, well above seismic resolution, to 20 meters, well below seismic resolution. The effects of fracture spacing and length are related to velocity anisotropy and seismic coda density, spacing, and intensity.

Phase 2 tests the seismic response to the addition of less idealized vertically fractured clusters within the center subdomain. Clusters are added in pairs to the model and are evenly spaced within the model. To better mimic natural fracture networks that are characterized by fracture density distributions, the clusters in this section have fracture spacing that exponentially decreases toward the center of the cluster. This creates areas within the model between clusters that are fracture free and areas in the center of clusters with high fracture density (Figure 4.6, left). This non-uniform fracture spacing varied further with changes in the number of fractures within each cluster and the spacing between each cluster. The outcome of these alterations are then related back to the wavefield and seismogram features of uniform variation in fracture spacing within a single idealized cluster described in the Phase 1.

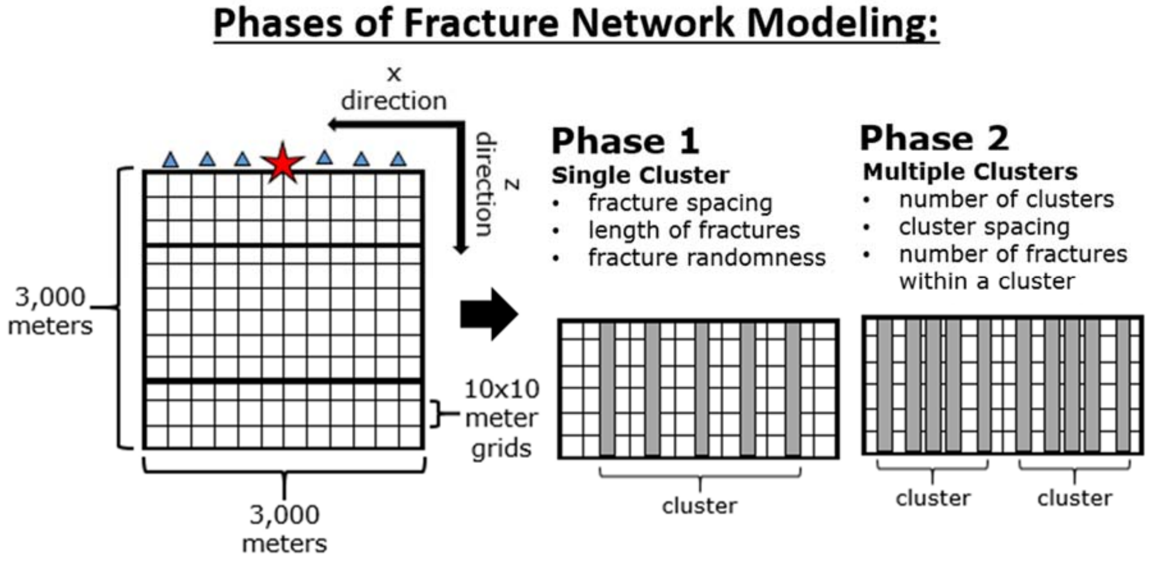

Figure 4.6: Parameters of 2D model construction and steps of fracture cluster modeling. A wave generated by a seismic source, shown as a red star, propagates through the model and recorded by receivers, shown as blue triangles (left). The model is divided into three horizontal initially isotropic layers. The top and bottom layers remain isotropic, while the center isotropic medium, represented by the light colored grids, is populated with vertical fractures of various parameters, represented by the dark colored grids (right).

Seismic Response to a Modeled Fracture

Figure 4.7 breaks down the wavefield response to an individual fracture so that, going forward, it will be clear what each feature described in chapter 2 looks like in modeled results. The wavefield snapshot (left) captures the interaction of the wavefield with the fractures after 0.44 seconds of modeled wave propagation time. The downgoing direct P-wave is delineated in orange, and the slower direct S-wave above is delineated in yellow. The vertical red lines represent the locations of the two fractures evenly spaced within the center interval of the model. The pair of mode converted S-reflections off of each fracture is delineated in light blue and form a "V" shape around their respective fractures. These features are present because the time elapsed since the direct P-wave interacted with the top of the fracture causing mode conversion is longer than the time elapsed since the interaction with the bottom of the fracture. It is important to mention that the arm of the "V" shape on the side of the fracture facing the source, centered at the top of the model, is noticeably stronger than the arm from the non-source facing side of the fracture.

P-wave and S-wave seismic diffraction coda are only generated on the side of the fracture facing the source and are delineated in purple and green, respectively. The P-wave coda appear below the fractures because they are created when the P-wave wavefront first contacts the fracture and continues to grow in horizontal extent as it travels along the length of the fracture. This phenomenon can be seen with the S-wave coda above that has just formed and is beginning to travel along the source-facing side of the fracture. Once the P-wave has passed below the fracture, the P-wave coda ceases horizontal growth but continues to propagate directly down into the model with the P-wave wavefront.

The seismogram (right) shows the wave energy collected by the receivers at the top of the model. The direct P-wave and its reflection off of the slightly absorbing model boundary is delineated in orange, whereas the mode converted component of P-wave reflection off of the model is delineated in brown. The direct S-wave is delineated in yellow and, again, the vertical red lines represent the locations of the two fractures within center interval of the model. The hyperbolic P-reflections off of the top and bottom of each fracture are highlighted in purple and light blue, respectively, and the hyperbolic S-wave reflections off of the top of the fractures are highlighted in green. The S-reflection off of the base of the fractures was not recorded because it had not propagated back up to the receivers before model propagation ended at 0.752 seconds. These reflections are attributed to the unnatural width of the fractures and should be replaced by more incoherent diffractions as fractures are thinned. It is important to note that the seismograms have been gained seven times more than the snapshots because most energy reflects between the fractures and does not escape to the surface to be recorded.

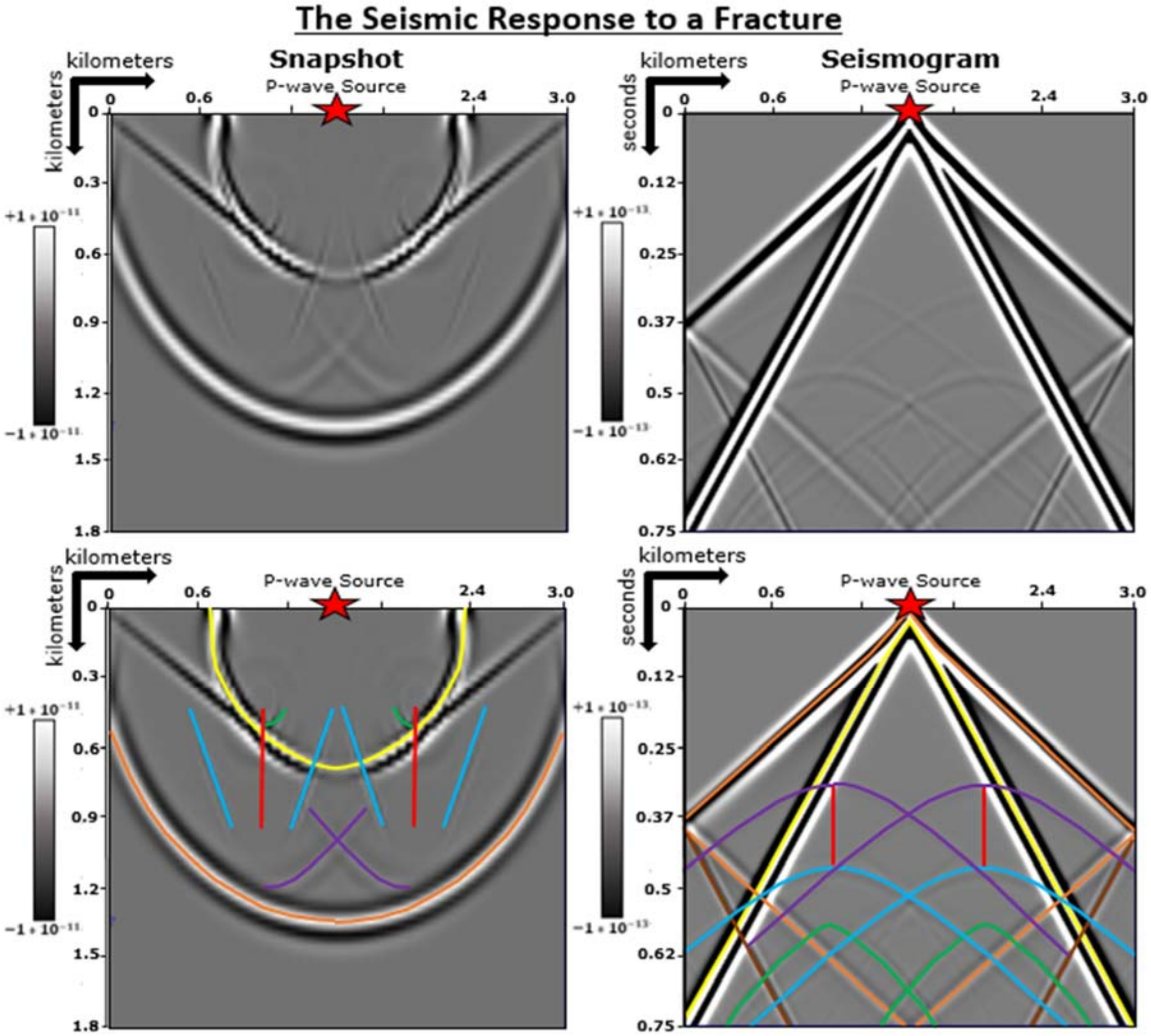

Figure 4.7: An annotated explanation of the seismic response to a vertical fracture. The snapshots (left) capture the interaction of the wavefield with two vertical fractures at a specific moment in time, and the seismograms (right) show the wave energy collected by the receivers at the top of the model. In the bottom annotated row, the two vertical fractures are delineated by red lines, the P-wave wavefront is delineated in orange, and the S-wave wavefront is delineated in yellow. The seismograms also show a P to S-wave mode converted reflection off the model boundary in brown. In the snapshot only, mode converted “V” shaped fracture reflections are shown in light blue, and P-wave and S-wave coda are shown in purple and green, respectively. In the seismogram, the upper and lower P-wave reflections off of the top and bottom of each fracture are shown in purple and light blue, respectively, and the S-wave top of fracture reflection is shown in green. Note that the seismograms have been gained seven times more than the snapshots.

SUMMARY

This chapter details the steps to modeling individual fracture attributes from model set up to what to examining resulting images. Using SWP3D, the wave propagation parameters of the type of wave equation used, dimensions modeled, type of wave propagation, and type of time stepping are defined, based upon the theory outlined in chapter 3 and in De Basabe (2009). Next, the steps were shown to determine appropriate model parameters for the source type and location, location of receivers, and absorbing boundary type. The modeled mesh was then given physical parameters of extent, velocity, and density. Trial and error was the main process used in this section to determine optimal parameters specific to the objectives of this study. Model run time was defined to minimize the real time in which these complex models take to complete. Grid refinement was done to ensure the resulting wavefields contained only modeled information and not numerical error. The physical model was completed with the definition of fracture parameters using the theory outlined in chapter 3. Lastly, the scope of this study was divided into two phases of fracture network attribute alteration. The seismic response to individual fractures was diagrammed so that the results in the following chapter may be more easily understood.

Chapter 5: Fracture Network Modeling Results

PHASE 1: SINGLE FRACTURE CLUSTER

Visual Comparison

Phase 1 of fracture network attribute modeling tests the seismic response to a single idealized vertically fractured cluster. This phase begins with infinite fracture spacing, representing an isotropic medium. Next, the center subdomain is populated with a single cluster containing evenly spaced, parallel, vertical, 10 meter-wide gas-filled fractures. The uniform spacing between each fracture was decreased from 1000 meters, allowing for only 2 fractures in the cluster, to 10 meters, allowing for 150 fractures in the cluster. The results of phase 1 are displayed in the following figures, with Figures 5.1 and 5.2 showing all unannotated and annotated wavefield snapshots, respectively, and Figures 5.3 and 5.4 showing all unannotated and annotated seismograms, respectively.

The wavefield snapshot for the first case of an isotropic medium with infinite fracture spacing is located in the top left corner of Figures 5.1 and 5.2. In an isotropic model, the P-wave and S-wave wavefronts should have a semi-circular shape, indicating that there have been no features for the waves to interact with during their traverse of the model. Isotropy is confirmed by measuring to determine that the distances traveled by the P-wave are equal in the x and z directions. This distance is a little more than 1500 meters in both directions. The second model from the left on the top row contains a cluster of two fractures spaced 1000 meters apart, even though only one fracture is visible in this quadrant of the model. The location of the fracture can be discerned from the wavefield events diagramed in Figure 4.7 of chapter 4 and highlighted in Figure 5.2. The fracture is centered within the mode converted S-wave “V” shape, delineated in blue, and directly above the left-most end of the P-wave coda, delineated in purple, and height of the fracture is equal to the vertical extent of the mode converted “V” shape. As the number of fractures within the cluster increases from left to right across the top row, a set of fracture wavefield events indicates the vertical extent and location of each fracture within the model, though some events cannot be seen in this quadrant of the model.

The left-most model in the center row of Figures 5.1 and 5.2 contains a cluster of 14 fractures spaced 190 meters apart. At this point it becomes difficult to discern all fracture wavefield events, but the stronger source-facing side of the mode converted “V” shape is still visible and indicates the location and vertical extent of each of the 7 fractures present in this quadrant of the model. The same is true for the second model from the left that contains a cluster of 18 fractures that have a spacing equal to the wavelength of 150 meters. The two models on the right contain fractures spaced less than the wavelength apart, and it is no longer possible to identify the location or spacing of individual fractures due to interference among each fracture’s wavefield events. From these right most models, it becomes more apparent that the mode converted “V” shaped features do not leave the fractured interval as the coda do, but instead remain as trapped energy between the fractures. This can be seen by looking between and below the yellow dotted lines indicating the location of the interval containing fractures. Between the yellow lines, there is a distinct linearity to the wavefield events, and the linear features are at an angle similar to that of the two models on the left, while below the lower-most yellow line, there exists only arcing coda energy.

When fracture spacing within the cluster decreases to less than one-half of the wavelength of 70 meters, coda energy becomes trapped within the fractured interval. This energy cannot continue to propagate out of the fractured interval without encountering another fracture’s wavefield events or the fracture itself. This is confirmed in the two models on the left of the bottom row that contain only faint reverberated events visible below the lower-most yellow dotted line. When fractures are spaced below seismic resolution, or one-fourth of the wavelength – 40m, no wavefield events can escape reverberation within the fractured interval. This is evident in the two models on the right of the bottom row that contain no energy other than the P-wave wavefront propagating down into the model. Instead, an “X” shape can be seen between the yellow dotted lines and the P-wave and S-wave wavefronts, delineated in pink. This X is formed when the wide fractures become so closely spaced that they effectively act as a layered interface and produce reflected events at the top and bottom of the fractured interval.

With the addition of more closely spaced fractures within the cluster, the P-wave directional velocity anisotropy described in chapter 2 is expected to become apparent in the lower-most row of Figures 5.1 and 5.2. The S-wave remains unaffected by the presence of the fluid-filled fractures. It is difficult to tell if the P-wave wavefront velocity has slowed upon exiting the fractured interval because these 2D models only provide a viewpoint perpendicular to fracture strike. Therefore, it is necessary to compare the P-wave wavefront within and below the fractured interval delineated by the yellow dotted lines. Below the fractured interval, the P-wave has, theoretically, traveled parallel to the fractures during its propagation directly downward into the model. Within the fractured interval, however, the P-wave has propagated out at various angles through the fractures and is slowed in these directions. This is apparent in the right-most model of the bottom row that represents a horizontal transversely isotropic medium. The P-wave wavefront below the fractured interval is rounded and resembles the wavefront of the isotropic model in the top left corner, whereas the wavefront within the fractured interval appears to have been straightened because it is traveling slower and has not propagated as far as the wavefronts above and below it.

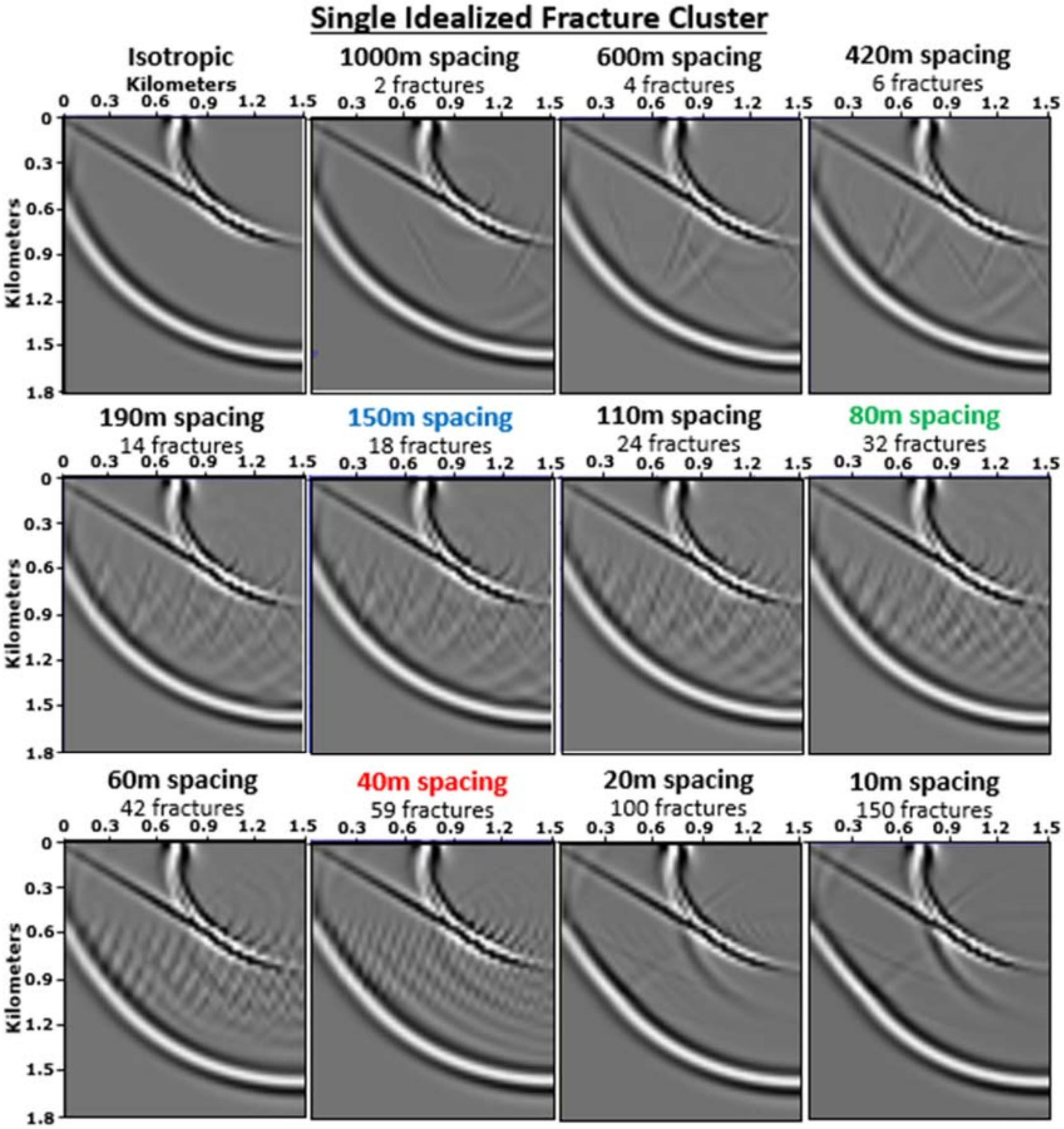

Figure 5.1: Results of Phase 1: Overview of wavefield snapshots, unannotated and showing the upper-left quadrant of the model only. Starting in the top left corner, the spacing between each fracture within a single cluster is uniformly decreased from infinite spacing, representing an isotropic medium, to 10 meter spacing in the bottom right corner, representing a horizontal transversely isotropic medium. The models containing fracture spacing equal to the wavelength, half of the wavelength, and one-fourth of the wavelength have their titles highlighted in blue, green, and red, respectively. Figure 4.7 in chapter 4 shows the scale bar for these wavefield snapshots.

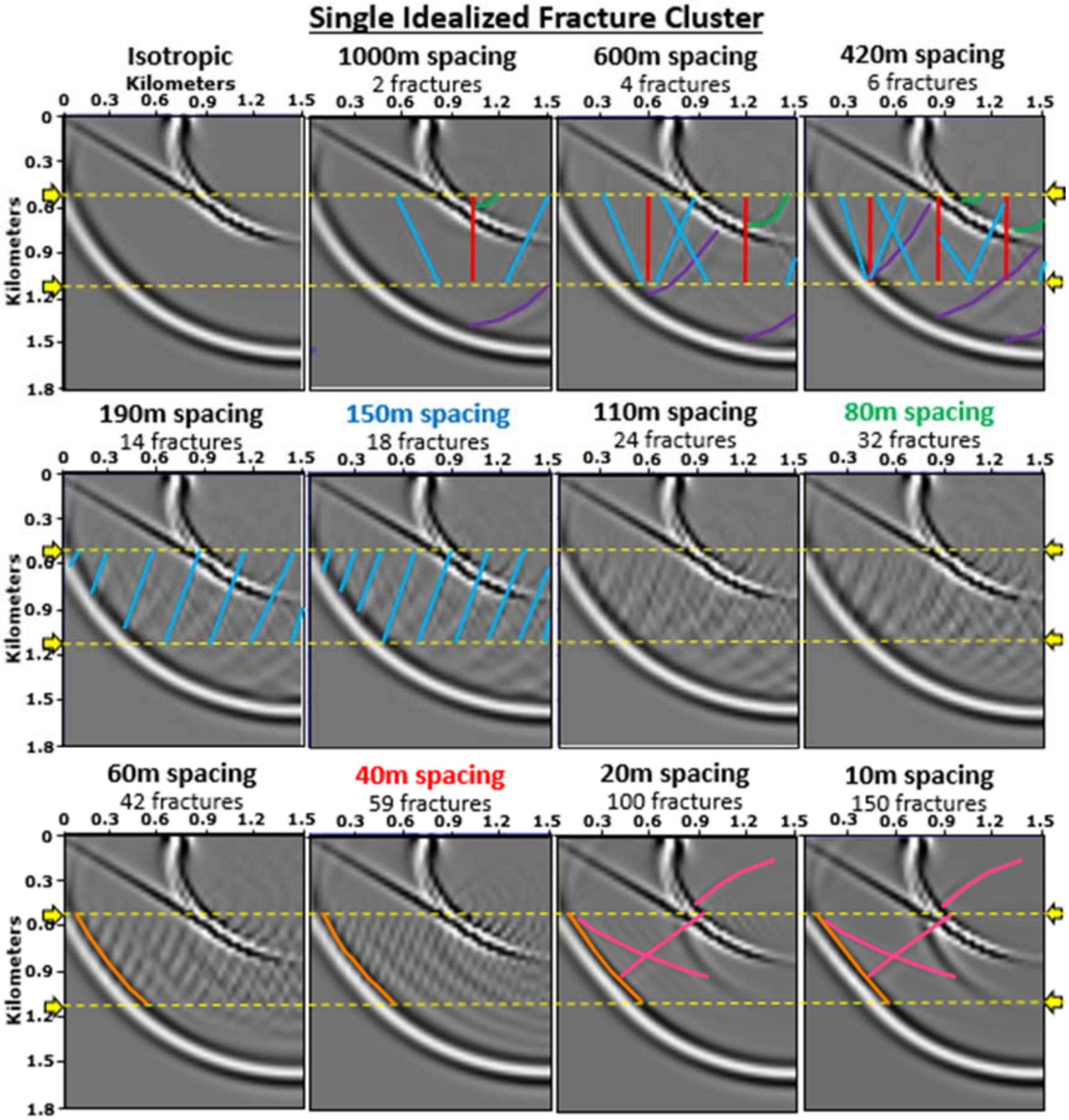

Figure 5.2: Results of Phase 1: Overview of wavefield snapshots with annotations. In each figure, the fractured interval is delineated by yellow dotted lines. The first row of models highlights the location and vertical extent of each fracture within the single cluster in red, S-wave coda in green, P-wave coda in purple, and mode converted S-wave “V-shaped” signature in light blue. Due to the increased fracture density in the second row of models, only the stronger source-facing side of the mode converted “V” shape is shown in blue to indicate the location of each fracture, when possible. The third row of models highlights the anisotropic straightening of the P-wave wavefront in orange and the effective reflections from the fractured interval in pink.

The seismogram for the first case of an isotropic medium with infinite fracture spacing is located in the top left corner of Figures 5.3 and 5.4. Isotropy of the host medium is confirmed by the presence of only the direct P-wave, the direct S-wave, and the P-wave reflection and mode conversion off of the sides of the model. The second model from the left on the top row contains a cluster of two fractures spaced 1000 meters apart, though again only one fracture is visible in this quadrant of the model. The location of the fracture can be discerned from the seismogram events diagramed in Figure 4.7 of chapter 4. The fracture lies centered between the apex of the two reflection hyperbolas formed from the top and base of the wide fracture, delineated by the solid bold yellow lines. As the number of fractures within the cluster increases from left to right across the top row, it quickly becomes difficult to separate individual fracture hyperbolas and, therefore, discern fracture location, extent, and spacing. The seismograms are shown with time along the z-axis creating the illusion that the left most fractures occur deeper within the model only because the P-wave wavefront requires more time to reach them.

The chaotic appearance of the interfering hyperbolas within and below the fractured interval can be seen in the two seismograms on the left of the center row in Figures 5.3 and 5.4. When fracture spacing within the cluster decreases below the wavelength of 150 meters, however, the chaotic pattern is replaced by a more regular crosscutting pattern, highlighted by the blue boxes in the two models on the right of the center row. Remember that at this point of fracture spacing decreasing below the wavelength in the snapshots, it became impossible to identify the location or spacing of individual fractures due to interference between each fracture's wavefield events. Also, at this point, it became apparent in the wavefields that the mode converted "V" shaped energy remained as trapped reverberations within the fractured interval. Therefore, the regularity of this crosscutting pattern in the models is due to uniformity in the shape of the coda from each fracture, which are regularly spaced and propagate downward with the same energy and at the same arcing angle.

As fracture spacing within the cluster is decreased below one-half of the wavelength of 70 meters, the time at which crosscutting energy appears begins to lengthen. This can be seen within the orange shaded regions of the models in the lowest row of Figures 5.3 and 5.4. At 60 meter fracture spacing, crosscutting energy appears half way through the fractured interval, delineated by the yellow dotted lines. Below 40 meter fracture spacing, crosscutting energy no longer appears within the fractured interval but, instead, directly below it. When fracture spacing within the cluster is decreased below half of the wavelength, coda energy can no longer propagate directly out of the fractured interval. Instead, the coda are subject to reverberation between the closely spaced fractures before escaping downward with much reduced energy.

When fractures within the cluster are spaced below seismic resolution of 40 meters, the wavefield snapshots indicated that the fractures effectively acted as a layered interface and produced a distinct reflection from the top and bottom of the fractured interval. In the seismograms in the two models on the right of the lowest row in Figure 5.4, distinct P-wave reflections are verified and lie directly below the yellow dotted lines. P-wave directional velocity anisotropy is, however, unapparent within the seismograms and will require 3D modeling to detect. An S-wave reflection off of the top of the fractured interval, delineated in pink, can be identified by a steep slope indicating slower velocity within the seismogram. The S-wave reflection can also be identified by its drop in amplitude at normal incidence to the source along the right edge of the figure where energy travels perpendicularly to the receivers. Lastly, a multiple of the P-wave reflection off of the top of the model, delineated in green, can be identified by its parallel slope to the primary P-refection and its double delay in time of the primary P-reflection.

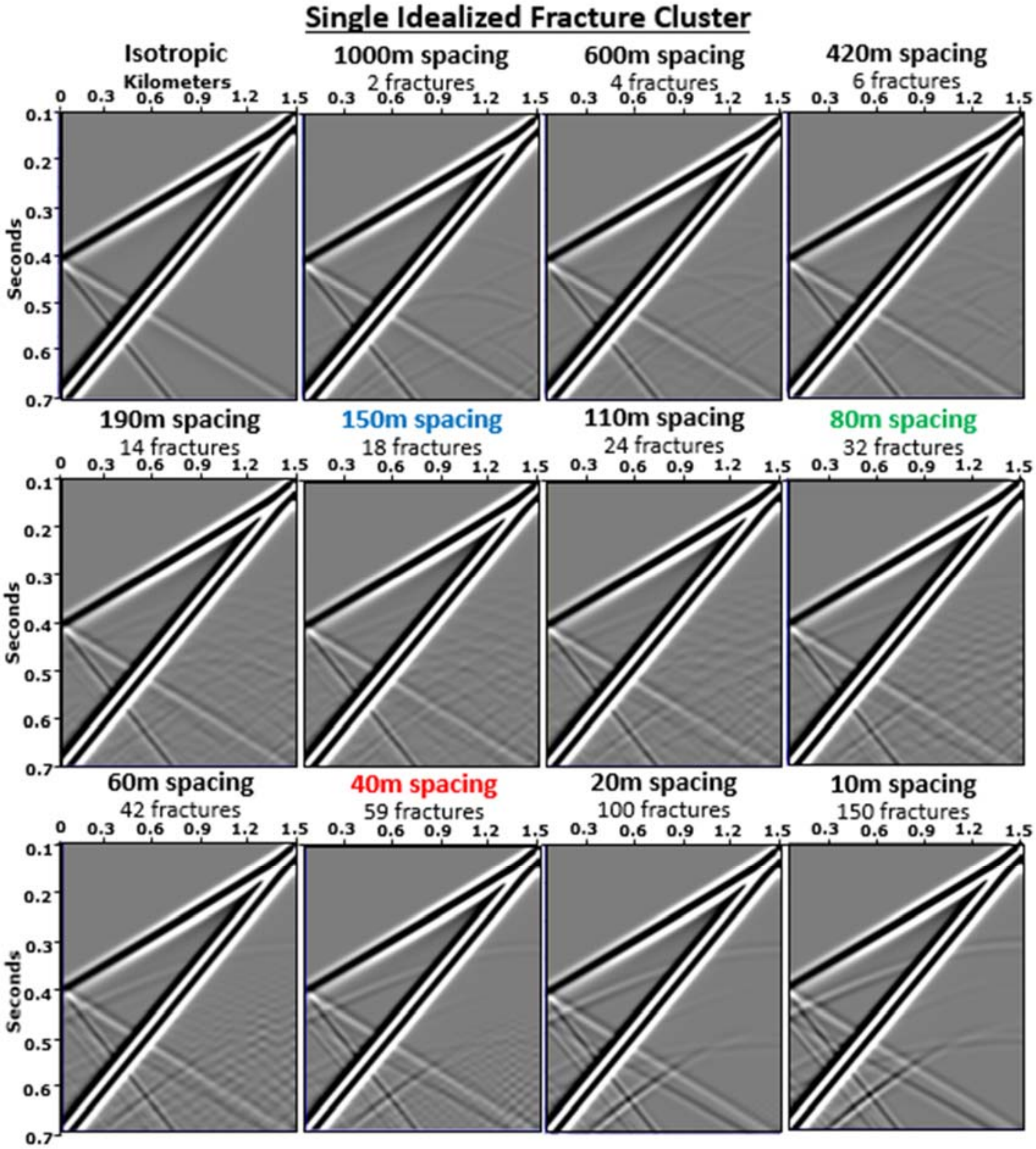

Figure 5.3: Results of Phase 1: Overview of seismograms, unannotated and showing the left quadrant of the model only. Starting in the top left corner, the spacing between each fracture within a single cluster is uniformly decreased from infinite spacing, representing an isotropic medium, to 10 meter spacing in the bottom right corner, representing a horizontal transversely isotropic medium. The models containing fracture spacing equal to the wavelength, half of the wavelength, and one-fourth of the wavelength are highlighted in blue, green, and red, respectively. Figure 4.7 in chapter 4 shows the scale bar for these seismograms.

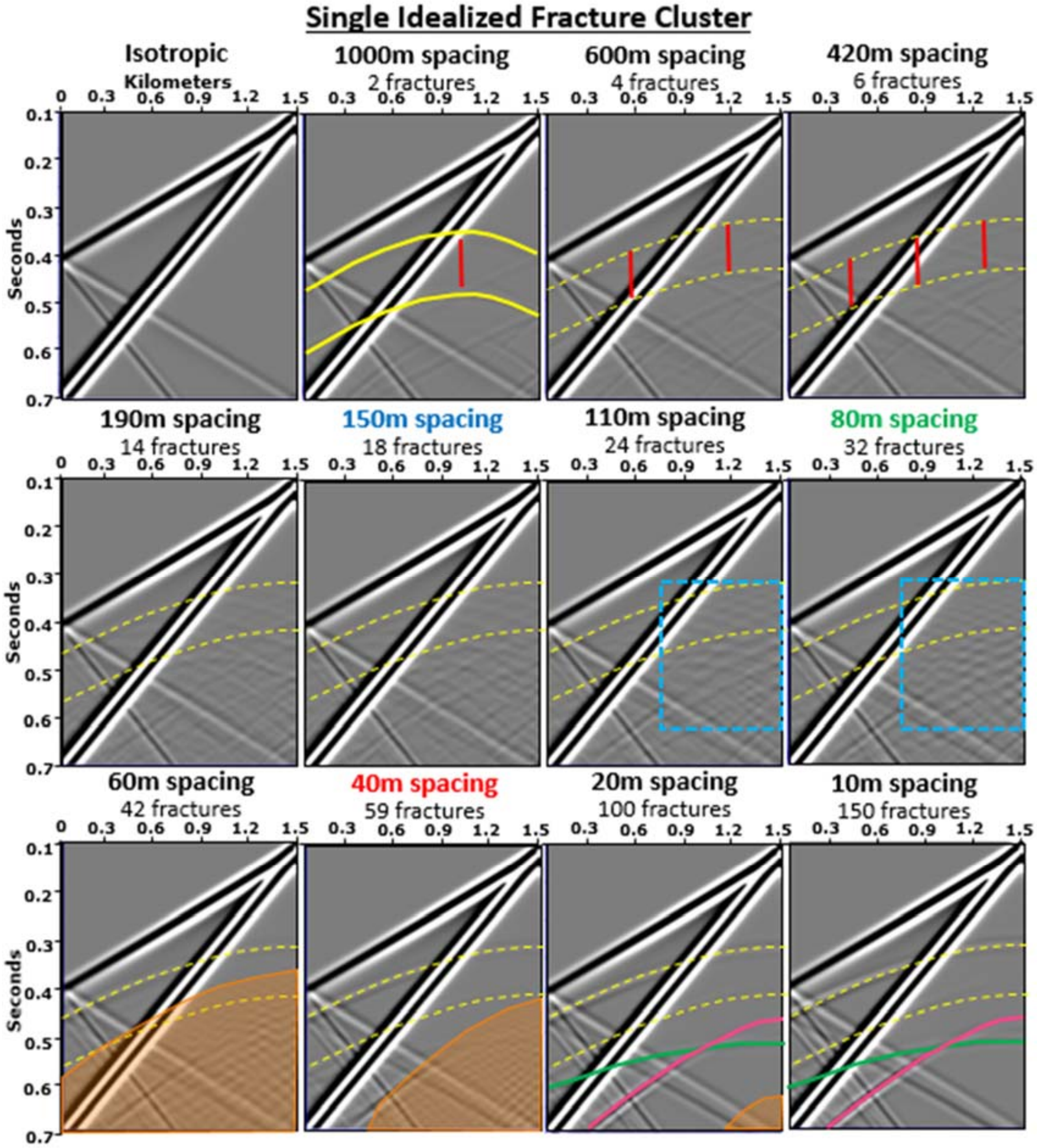

Figure 5.4: Results of Phase 1: Overview of seismograms with annotations. The first row of models highlights the location and vertical extent of each fracture in red. The solid bold yellow lines delineate individual reflection hyperbolas while the location in time of the fractured interval is delineated by yellow dotted lines. The first appearances of distinct fracture-related crosscutting energy is boxed in dotted blue lines, and the decrease in the extent of crosscutting energy with depth as fracture spacing decreases is shaded in orange. The pink line delineates the effective S-reflection off the top of the fractured interval, and the green line delineates the P-reflection multiple.

Sensitivity of Coda Crosscutting Signature

Effect of Uniform Fracture Spacing

The results of Figures 5.3 and 5.4 indicate that crosscutting energy patterns within a seismogram can indicate the presence of a fracture network whose fracture spacing is relatively small. The results above also indicate that this energy most often occurs in a location away from where the fractures are present. To gain more insight on the depth at which fracture related crosscutting energy appears in seismograms, its sensitivity to fracture spacing must be tested. The relationship between the first occurrence of crosscutting energy and uniform fracture spacing is analyzed in this subsection. Figure 5.5 shows all models with fractures spaced less than one-half of the wavelength, when this crosscutting phenomenon occurs. The depth of first occurrence has been delineated by the red dotted line in each model and written below each model after being converted from time using normal moveout velocities. The annotated depths in Figure 5.5 confirm that the depth at which crosscutting energy occurs exponentially decreases with a decrease in fracture spacing. This delay in first occurrence of crosscutting energy is the result of seismic coda reverberating more often between the more closely spaced fractures. The increased time required for this energy to escape the clustered interval causes the seismic coda to appear well below the true location of the fracture cluster.

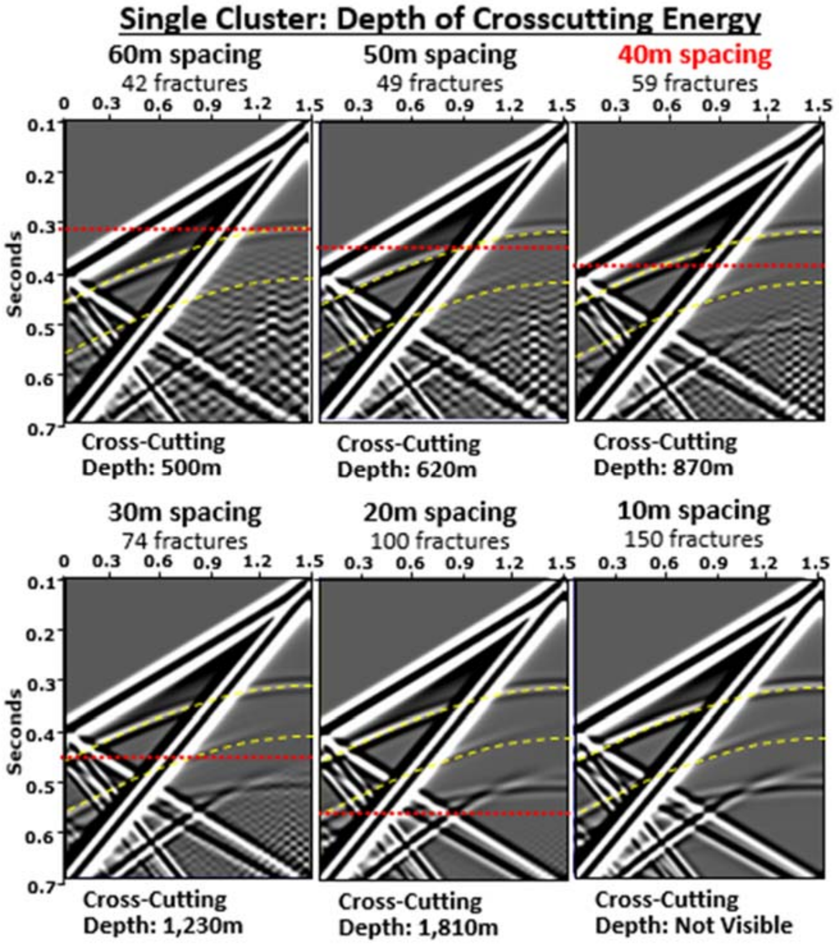

Figure 5.5: Analysis of Phase 1: Sensitivity of the depth of fracture-related crosscutting energy to decreased fracture spacing. The models have had double the amount of gain applied to help aid detection of the time and depth at which crosscutting energy first occurs. The location in time of the fractured interval is delineated by the yellow dotted lines, and the time at which crosscutting energy first appears is delineated by the red dotted lines. Using the defined background velocity and the normal moveout velocity of the reflection off of the base of the fractured layer, the time of first crosscutting energy is converted to depth below each model so that it can be more easily compared to fracture spacing. Again, the title of the model containing fracture spacing equal to one-fourth of the wavelength is highlighted in red.

Effect of Fracture Length

The analysis of Figures 5.5 lead to the hypothesis that the location of crosscutting energy is directly related to the degree of reverberation that the wavefield undergoes during is traverse of the fractured interval. A reasonable inference from this statement is that as fracture length decreases, crosscutting delay time should decrease and intensity should increase because fewer reverberations will occur within a shorter fractured interval. A literature review of this scenario, however, states that as fractures are shortened, scattered energy from a fractured interval will increasingly attenuate (Grandi-Karam, 2008). Upon shortening the fractures in this study from 500 to 20 meters, surprisingly little change in either energy amplitude or delay time of crosscutting can be seen (Figure 5.6). An explanation is that as the wavefront enters a corridor between fractures, it arrives incident upon the face of a fracture at an angle independent of fracture length. Therefore, only when fracture spacing changes does the angle at which the wavefront comes in contact with the fracture face change, resulting in a change of delay time. Closer examination of Figure 5.6 also reveals that, at all fracture spacings less than one-half of the wavelength and greater than an effective HTI medium, there is a slight crosscutting amplitude decrease when fractures are slightly above one-fourth of the wavelength, or 50 meters, and a slight amplitude increase when fractures are below one-fourth of the wavelength, or 20 meters. These fracture lengths most likely correspond to minimum and maximum lengths for constructive interference, respectively.

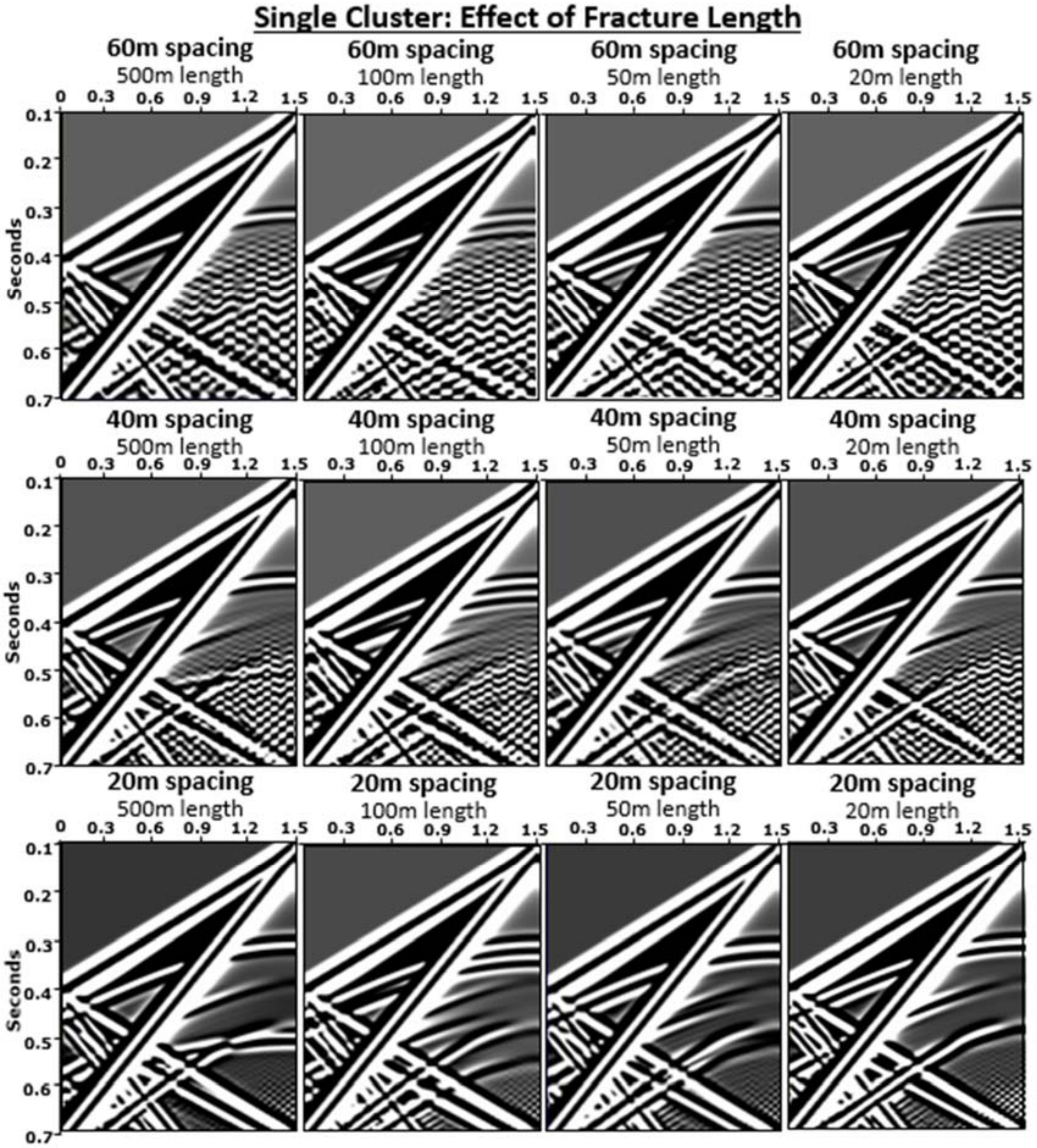

Figure 5.6: Analysis of Phase 1: Sensitivity of the depth of fracture-related crosscutting energy to decreased fracture length. The models have had triple the amount of gain applied to help aid detection of changes in crosscutting energy. As fracture length is decreased from 500m in the left-most column to 20m in the right-most column, little difference can be seen in the models of 60m, 40m, and 20m fracture spacing, from top to bottom, respectively. A slight drop in amplitude of crosscutting can be seen with all fracture spacings when fracture length is 50m and a slight increase in amplitude can be seen with all fracture spacings when fracture length is 20m.

Effect of Cluster Non-Uniformity

To further constrain the limits of discernibility of crosscutting energy, the single idealized cluster is randomized to better mimic fracture networks present in the subsurface. To do so, individual fractures within the cluster are randomly selected and moved from their uniformly spaced locations to arbitrary locations. If the new location fell on top of another fracture, the fracture being moved was deleted from the model. The number of fractures selected and moved was systematically increased from 3 to 36 in order to determine the limit of confident identification of crosscutting energy as an indication of the presence of a fracture cluster. Figure 5.7 depicts the change from a regular crosscutting pattern to incoherent hyperbolic events in the seismograms as fracture locations are randomized. The top-left model in Figure 5.7 is identical to the top-left model in Figures 5.5 and 5.6, and contains a single cluster of 42 fractures that are each uniformly spaced 60 meters apart. This analysis indicates that crosscutting is visually detectable when the cluster of 42 fractures contains less than 12 randomized fractures, or 28% non-uniformity, which could exist in natural rock formations.

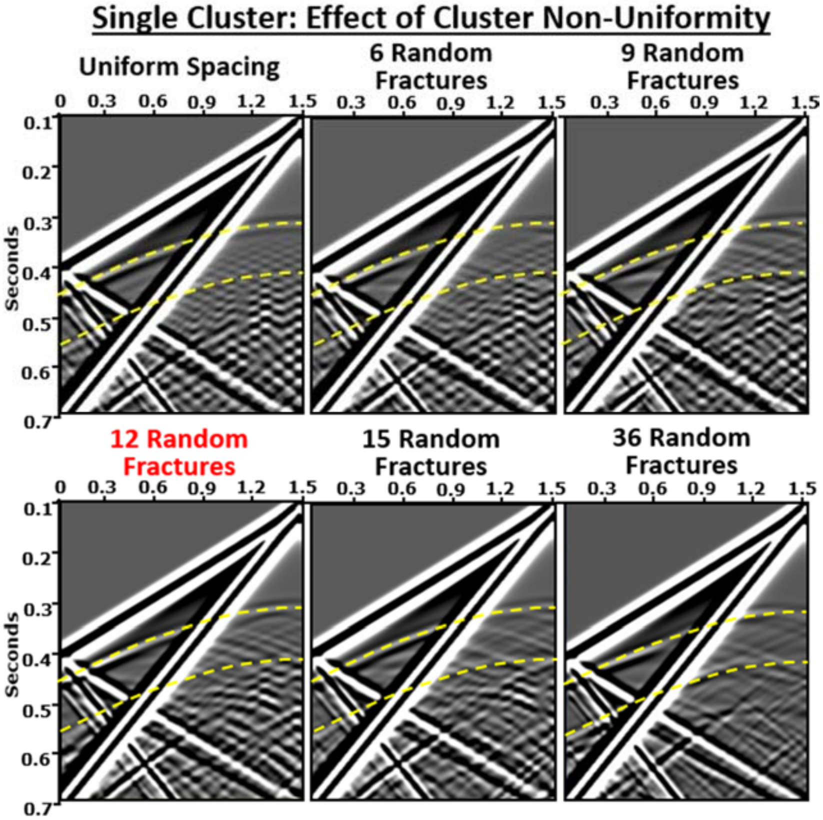

Figure 5.7: Analysis of Phase 1: Sensitivity of fracture-related crosscutting energy to the addition of non-uniformities to the cluster. The models have had double the amount of gain applied to help aid detection of changes in crosscutting energy. The location in time of the fractured interval is delineated by the yellow dotted lines. As the number of fractures randomly moved to new locations within the cluster increases, the regular shape of the crosscutting pattern fades, making it difficult to identify confidently. The limit of the discernibility of crosscutting energy is 12 random fractures within the cluster of 42 fractures, highlighted in red.

PHASE 2: MULTIPLE FRACTURE CLUSTERS

Visual Comparison

Phase 2 of fracture network attribute modeling tests the seismic response to the addition of less idealized vertically fractured clusters within the center subdomain. In this phase, clusters are added in pairs to the model and are evenly spaced within the model. To better mimic natural fracture networks, the clusters have fracture spacing that exponentially decreases toward the center of the cluster. This creates areas within the model between clusters that are fracture free and areas in the center of clusters with high fracture density. The results of phase 2 are displayed in the following figures, with Figure 5.8 showing unannotated wavefield snapshots and corresponding seismograms and Figure 5.9 showing annotated wavefield snapshots and corresponding seismograms.

The wavefield snapshot for the first case of a single cluster of fractures with exponentially decreasing fracture spacing toward the center of the cluster is located in the top left corner of Figures 5.8 and 5.9. This cluster contains 13 gas-filled fractures that are spaced from right to left as follows: 320m, 160m, 80m, 40m, 20m, 10m, 10m, 20m, 40m, 80m, 160m and 320m. The center of the cluster is defined by the fracture located between the two 10 meter spacings. Though the cluster is centered in the model, with the location of highest fracture density indicated by the red line in Figure 5.9, only the left half of the cluster can be seen in this quadrant of the model. The location of highest fracture density is discernible by looking at how the wavefield features from each fracture interact. On the left side of the figure, distinct mode conversion and P-wave coda can be seen indicating the presence of a single fracture. On the far right side, wavefield events from the more closely spaced fractures are destructively interfering and appear as more diffuse energy with blurred crosscutting coda below the densest point within the cluster. In the seismogram below, however, chaotic reflection hyperbolas dominate, and little difference can be seen between the left and right side of the model to indicate the location of highest fracture density.

With the addition of evenly and equally spaced clusters to the model, it becomes more difficult to differentiate areas of well-formed fracture wavefield features from areas of destructive interference. This is the result of maintaining a large space between each cluster, which resulted in the systematic removal of the two outward-most fractures with the greatest fracture spacing from each cluster. Therefore, the second model from the left contains two clusters spaced 310 meters apart that contain 11 fractures each that are spaced from left to right as follows: 160m, 80m, 40m, 20m, 10m, 10m, 20m, 40m, 80m, and 160m. The second model from the right contains four clusters again spaced 310 meters apart that contain 9 fractures each that are spaced from left to right as follows: 80m, 40m, 20m, 10m, 10m, 20m, 40m, and 80m. Lastly, the right-most model contains six clusters again spaced 310m apart that contain 7 fractures each that are spaced from left to right as follows: 40m, 20m, 10m, 10m, 20m and 40m.

In the seismograms below, the chaotic nature of the hyperbolas again makes it difficult to extract useful information about cluster attributes. The second model from the left on the bottom row containing two clusters has the most crosscutting energy in the location between the two clusters, while the next model over to the right containing 4 clusters is dominated by intervals of destructive interference with little energy and constructive interference with brighter hyperbolic shapes. The seismogram farthest to the right containing 6 clusters has constructive interference at the top and base of the fractured interval, highlighted by the yellow arrows, and destructive interference within and below the fractured interval that begins to form the coherent layer-like reflections noted in the bottom-right model of Figure 5.4. It is interesting that these reflection features are present within this model containing a total of only 42 fractures, while 60 evenly spaced fractures were needed within a model to delineate both the top and bottom of the fractured interval.

Though the fracture-related wavefield and seismogram features of Figures 5.8 and 5.9 fail to convey much about the clusters within, two important wavefront features are able to differentiate areas of high and low fracture density. Below the center location of each cluster, delineated in red in Figure 5.9, a bend forms in the P-wave wavefront, delineated in blue. As the number of clusters increases, the bends become more apparent, and the wavefront is transformed into a polygonal shape. These bends are formed in the same way that the P-wave wavefronts of the bottom row in Figure 5.2 form and are, therefore, a type of heterogeneous anisotropy.

Below the location of highest fracture density within each cluster, there is also a noticeable decrease in P-wave wavefront amplitude at the point of maximum curvature within the bend. The decrease in amplitude is most apparent in the model farthest to the right with the largest number of clusters, though those clusters contain the smallest number of fractures. Because cluster spacing has been maintained and a decrease in fracture number should not increase amplitude attenuation, this phenomenon is attributed to the presence of only very closely spaced fractures within these 6 clusters. When the hyperbolas from reflections off of the top of fractures within the clusters are traced, shown in orange in Figure 5.9, the heterogeneous bends are faintly visible. It is unclear if these bends are the result of anisotropy or possibly the individual hyperbolas from the fractures with the largest spacing on each end of the clusters.

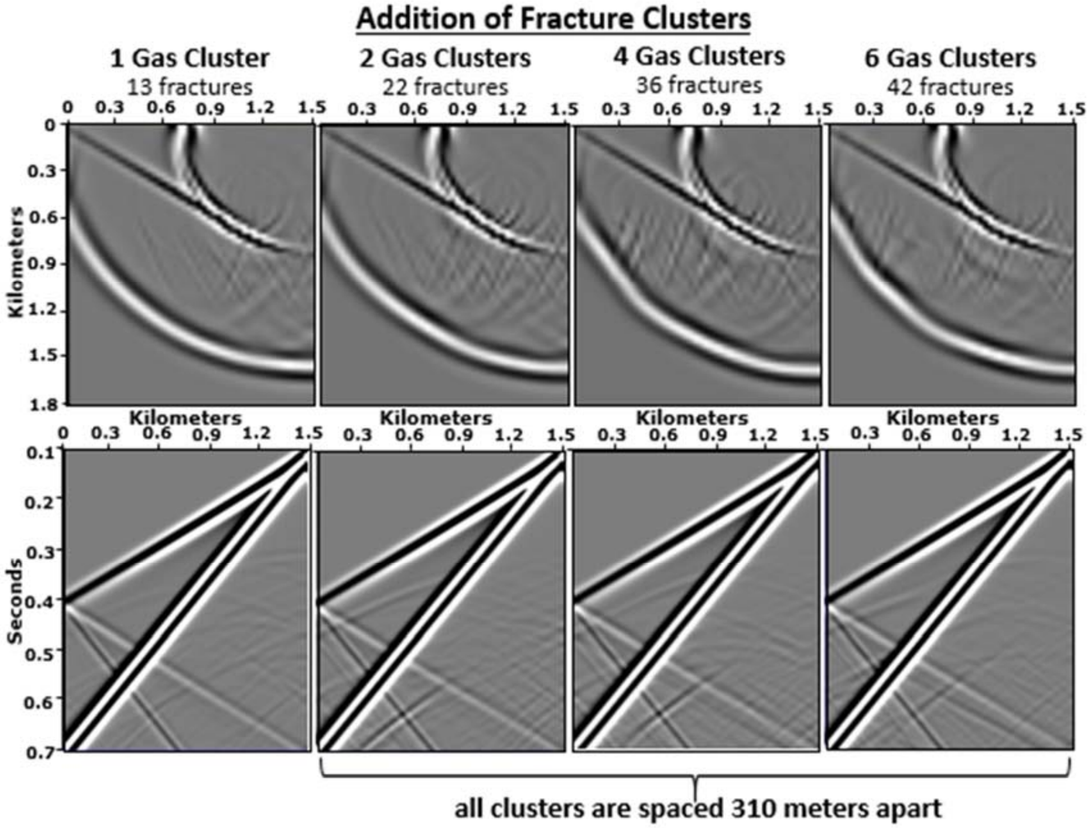

Figure 5.8: Results of Phase 2: Overview of wavefield snapshots and seismograms, unannotated and showing the left quadrant of the model only. The left-most model contains a cluster of 13 gas-filled fractures that are spaced from left to right as follows: 320m, 160m, 80m, 40m, 20m, 10m, 0m, 10m, 20m, 40m, 80m, 160m, 320m, and there are 810m buffers between the last fracture on each end and the edge of the model. The second model from the left contains two clusters spaced 310m apart that contain 11 fractures each that are spaced from left to right as follows: 160m, 80m, 40m, 20m, 10m, 0m, 10m, 20m, 40m, 80m, 160m, and there are 620m buffers between the last fracture on each end and the edge of the model. The second model from the right contains four clusters spaced 310m apart that contain 9 fractures each that are spaced from left to right as follows: 80m, 40m, 20m, 10m, 0m, 10m, 20m, 40m, 80m, and there are 250m buffers between the last fracture on each end and the edge of the model. The right-most model contains six clusters spaced 310m apart that contain 7 fractures each that are spaced from left to right as follows: 40m, 20m, 10m, 0m, 10m, 20m, 40m, and there are 100m buffers between the last fracture on each end and the edge of the model.

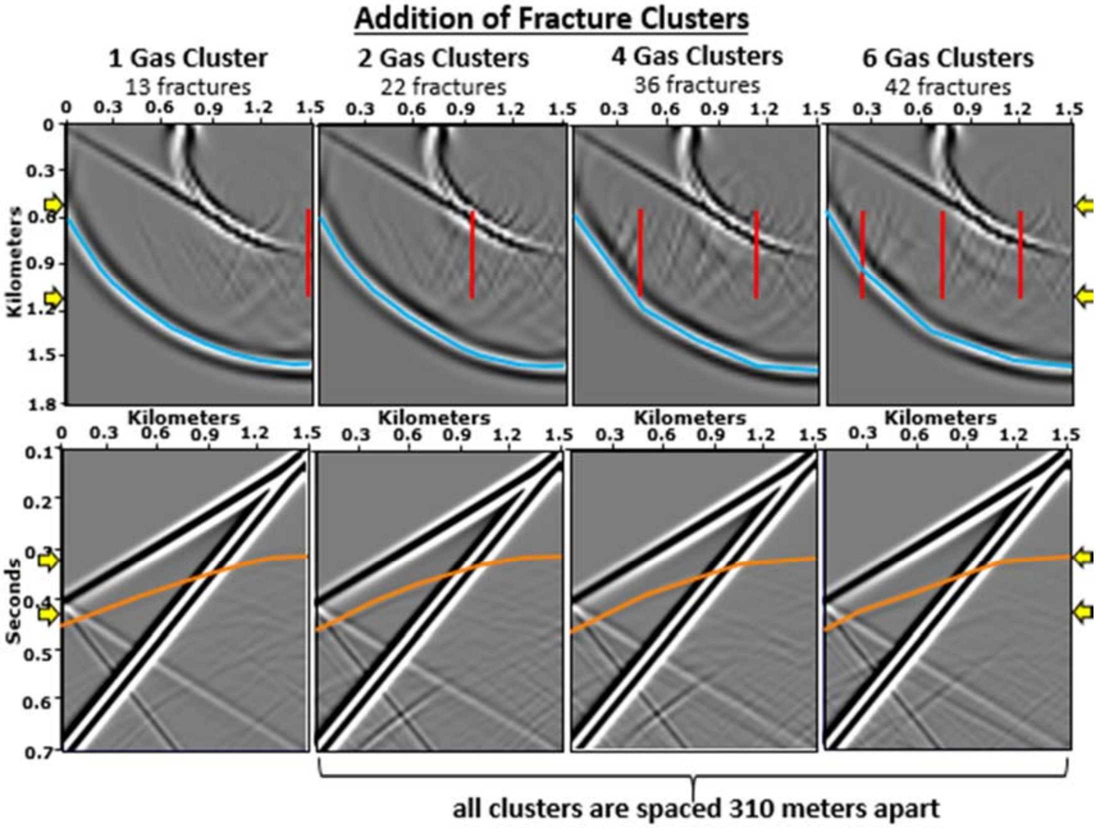

Figure 5.9: Results of Phase 2: Overview of wavefield snapshots and seismograms, with annotations. The yellow arrows indicate the location of the fractured interval. In the wavefield snapshots above, the red lines show the center location of each cluster where fracture density is greatest and do not represent a particular fracture. The P-wave wavefront is delineated in blue to emphasize the bends, or heterogeneous anisotropic pattern, that form below the densest portion of each cluster. In the seismograms below, the reflection off of the top of the fractured interval is delineated in orange to again emphasize the heterogeneous anisotropy produced by each cluster.

Sensitivity of Heterogeneous Anisotropy

Effect of Fracture Density

To better understand the limitations of using heterogeneous anisotropy to identify fracture clustering, its sensitivity to cluster parameters must be tested. The number of fractures needed within a cluster to form heterogeneous bends and amplitude variation in the P-wave wavefront is analyzed in this subsection. The results are displayed unannotated and annotated in Figures 5.10 and 5.11, respectively. The first column of Figures 5.10 and 5.11 is identical to the last column of Figures 5.8 and 5.9, and contains 6 clusters spaced 310 meters apart that contain 7 fractures each. This model had the most exaggerated heterogeneous anisotropy in its P-wave wavefront, delineated in blue in Figure 5.9, and in its upper fractured interval reflection, delineated in orange.

The column second to the left was generated by removing the outermost fracture from each side of each cluster, resulting in 6 clusters of 5 fractures that have the same exponential decrease in fracture spacing described in the section above. Because the number of fractures in each cluster has decreased but the number of clusters remains the same, cluster spacing has increased to 410 meters. In the wavefield snapshot above, there is a noticeable decrease in the number of fracture-related wavefield events surrounding the center location of each cluster, yet there appears to be no change in the severity of the bends in the P-wave wave front. The decrease in amplitude at point of maximum curvature in each bend does appear to have lessened, however. In the snapshots below, however, it becomes apparent that the bends in the upper fractured interval reflection are due to the adjoining curves of interfering hyperbolas from singular fractures and not an indication of anisotropy.

The second column from the right in Figures 5.10 and 5.11 was generated by removing two more outer fractures from each cluster, resulting in 6 clusters spaced 470 meters apart with 3 fractures in each. Again, there is a noticeable decrease in the number of wavefield events in the wavefield snapshots above but, in this case, there is also a decrease in the severity of the bends in the P-wave wavefront and a further decrease in the amplitude dampening at the elbow of each bend. In the seismograms below, cluster spacing has increased such that it is now possible to pick out some of the brighter individual fracture hyperbolas, further confirming that it is the adjoining of hyperbolic curves that creates the bends in the upper fractured interval.

The column farthest to the right was generated by removing all but the centermost fracture from each cluster, essentially modeling 6 individual fractures spaced 510 meters apart. It is at this point that there is no visual indication of heterogeneous anisotropy in the amplitude or shape of the P-wave wavefront in the snapshot above or in the seismogram below. Therefore, the limit to the number of fractures within a cluster that can cause heterogeneous anisotropic characteristics is 3 fractures. It is important to remember that the fractures being modeled are 10 meters wide and, therefore, the more realistic sensitivity of heterogeneous anisotropy is that of 30 meters of fracture infill, for every 80 meters of background material.

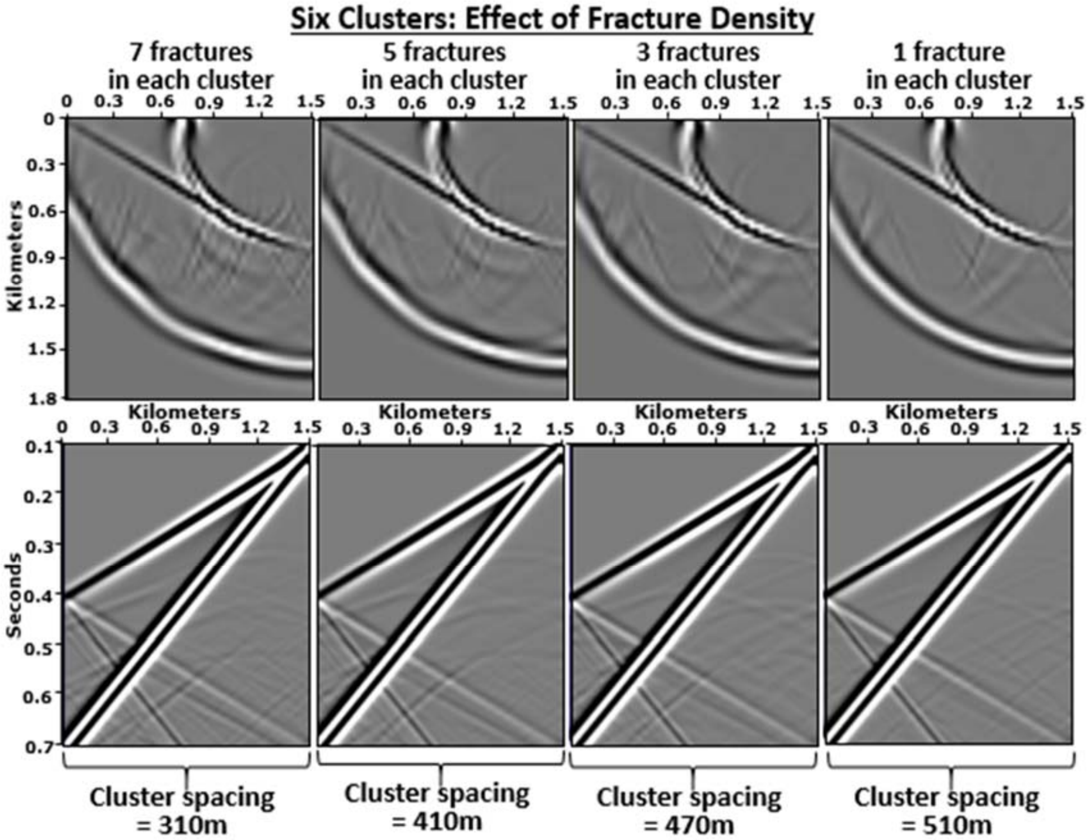

Figure 5.10: Analysis of Phase 2: Sensitivity of heterogeneous anisotropy to a decrease in fracture density within a cluster, unannotated and showing the left quadrant of the model only. The left-most model is the same as the right-most model in Figures 5.8 and 5.9 and contains six clusters spaced 310m apart that contain 7 fractures each that are spaced from left to right as follows: 40m, 20m, 10m, 10m, 20m, 40m, and there are 100m buffers between the last fracture on each end and the edge of the model. The second model from the left contains the same six clusters but with the two outward most fractures removed from each cluster, resulting in only 5 fractures in each cluster and a cluster spacing of 410m. The second model from the right contains the same six clusters but with the four outward most fractures removed from each cluster, resulting in only 3 fractures each cluster and a cluster spacing of 470m. The right-most model contains the same six clusters but with the six outward most fractures removed from each cluster, resulting in only 1 fracture each cluster and a cluster spacing of 510m.

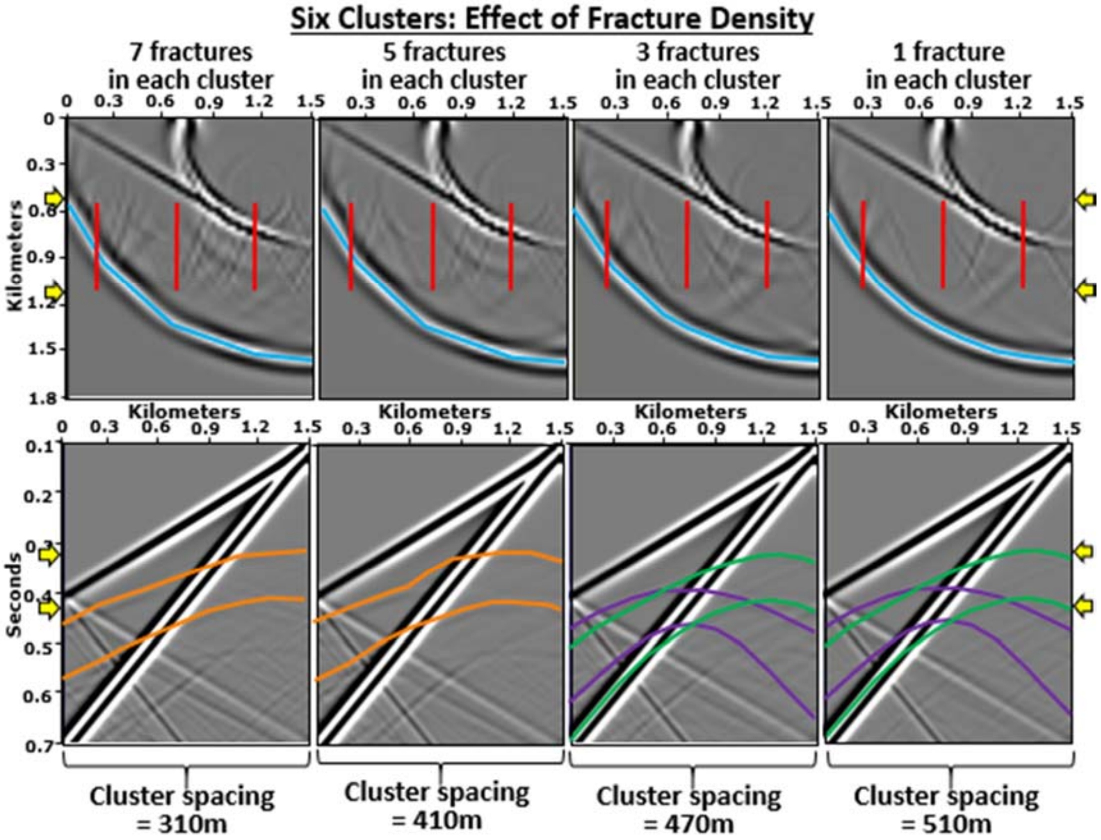

Figure 5.11: Analysis of Phase 2: Sensitivity of heterogeneous anisotropy to a decrease in fracture density within a cluster, with annotations. The yellow arrows indicate the location of the fractured interval. In the wavefield snapshots above, the red lines show the center location of each cluster where fracture density is greatest, and the blue lines highlight the P-wave wavefront bends, or heterogeneous anisotropy. In the seismograms below, the reflections off of the top and bottom of the fractured interval are delineated in orange in the left two models to again highlight the heterogeneous anisotropic bends. In the right two models, fracture density is not great enough to produce a coherent reflection off of the fractured interval and, instead, the hyperbolas from the right most cluster are delineated in green, and the hyperbolas from the center cluster are delineated in purple. The left most cluster is too close to the boundary of the model to produce coherent hyperbolas due to model edge effects.

Effect of Cluster Spacing

The spacing needed between each cluster to form heterogeneous bends and amplitude variation in the P-wave wavefront is analyzed in this subsection. The results are displayed unannotated and annotated in Figures 5.12 and 5.13, respectively. The first column of Figures 5.12 and 5.13 is identical to the first column of Figures 5.10 and 5.11, and contains 6 clusters spaced 310 meters apart that contain 7 fractures each that have an exponential decrease in fracture spacing from 40m between the outer-most fractures to 10m between the inner-most fractures. The center column contains the same six clusters but with a cluster spacing decreased to 150 meters, allowing for 16 fractures in each cluster. The amplitude decrease in the P-wave wavefront is still readily apparent in the wavefront snapshot above, but the bends within wavefront are less regular. In particular, the bend furthest to the left is most visible and appears to be twice as long as others further down in section from it.

The right column of Figures 5.12 and 5.13 contains the same six clusters again, but with a cluster spacing of 70 meters, allowing for 20 fractures in each cluster. At this point, there is very little amplitude variation, and only a small degree of bending in the P-wave wavefront. Instead, the effects of an effective horizontal transversely isotropic medium, described in the results of phase 1, become apparent in the velocity variation of the wavefront that propagates parallel to the fractures downward. The wavefront that travels through the fractures due to its angle of propagation. In the seismogram below, the effective reflection off of the top of the fractured interval is readily apparent, while the bottom reflection has not formed yet from constructive interference of reflection hyperbolas. Therefore, the lower limit to the separation that clusters can have and cause heterogeneous anisotropic characteristics is 150 meters, or the wavelength of the source used.

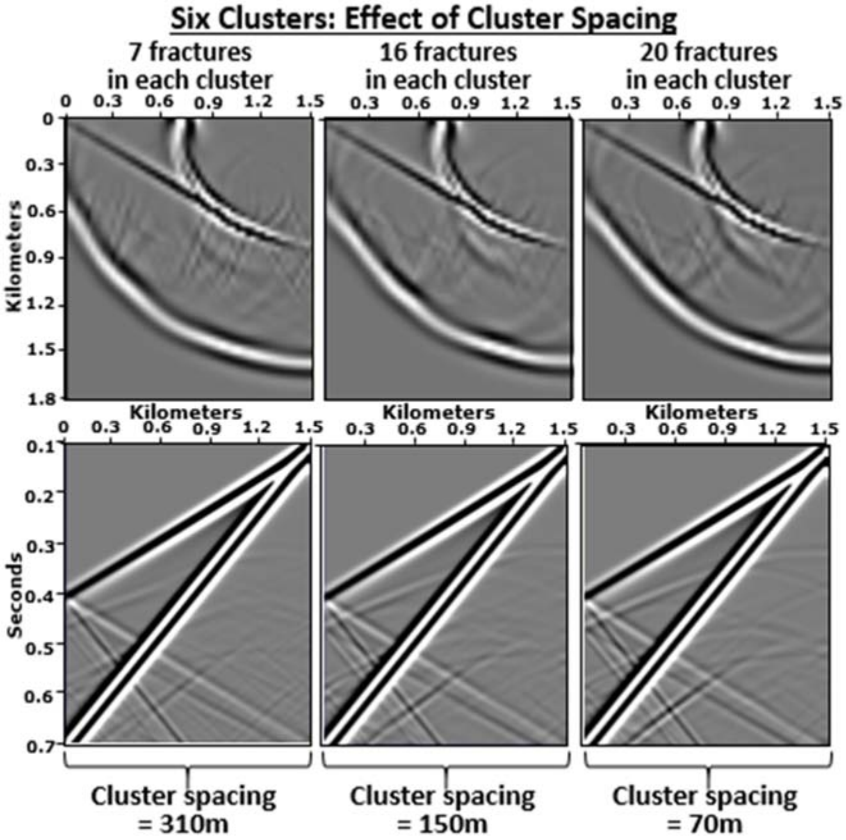

Figure 5.12: Analysis of Phase 2: Sensitivity of heterogeneous anisotropy to decreased spacing between each cluster, unannotated and showing the left quadrant of the model only. The left column is the same as the left-most model in Figures 5.10 and 5.11 and contains six clusters spaced 310m apart that contain 7 fractures each cluster. The center column contains the same six clusters but with a cluster spacing of 150m and 16 fractures in each cluster. The right column contains the same six clusters but with a cluster spacing of 70m and 20 fractures in each cluster.

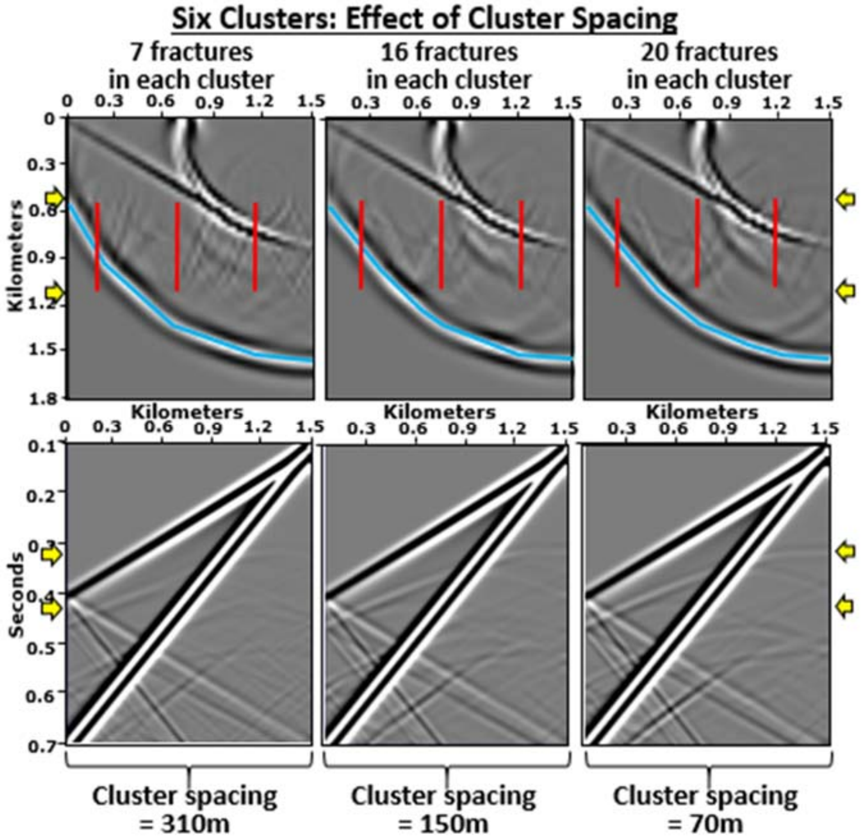

Figure 5.13: Analysis of Phase 2: Sensitivity of heterogeneous anisotropy to decreased spacing between each cluster, with annotations. The yellow arrows indicate the location of the fractured interval. In the wavefield snapshots, the red lines show the center location of the six clusters in each model and the blue lines highlight the P-wave wavefronts' bends, or heterogeneous anisotropy.

Single Idealized Cluster versus Multiple Realistic Clusters

As a final step to understanding the seismic response to fracture clustering, the difference in sensitivity of wavefield events to uniform and non-uniform fracture clusters is compared in this section. Only seismograms are compared because they are information available from seismic surveying and, therefore, show what information can realistically be obtained about fracture spacing from seismic data. The top-left model of Figure 5.14 is identical to bottom-left seismogram in Figures 5.3 and 5.4, though it has been gained three times more. This model contains a single cluster of 42 fractures uniformly spaced 60 meters apart. Because only one cluster is modeled in Phase 1, this cluster spans the width of the model, or 2880 meters. The bottom-left model is identical to the bottom-left seismogram in Figures 5.10 – 5.13, though it has again been gained three times more. This model contains 6 clusters spaced 310 meters apart that contain 7 fractures each that have an exponential decrease in fracture spacing from 40m between the outer-most fractures to 10m between the inner-most fractures. Though both models contain a total of 42 fractures, their seismograms are significantly different. The distinct crosscutting energy produced by the uniform cluster is an obvious indication of fracture clustering, but the non-uniformity of the multiple clusters with variable fracture density renders the seismogram almost useless for confident identification of cluster presence, properties, or location.

Though the differences between the seismograms in left column of Figure 5.14 are obvious when gained, before concluding on the sensitivity of a seismic wave's ability to detect uniform and non-uniform variations in fracture clustering, it is important to see how large of an effect adding noise has on the features outlined above. The right column of Figure 3.14 contains the same models but Gaussian noise has been added to each at a forgiving 500 signal to noise ratio. With a small amount of noise added, it becomes difficult to differentiate wavefield events other than the direct arrivals. Although identification of crosscutting energy is possible in the lower right corner of the upper seismogram, it is impossible to detect wavefield events truly indicative of fracture clustering in the lower seismogram. Therefore, crosscutting energy might not be an effective interpretation tool when dealing with natural, non-uniform fracture clusters within subsurface reservoirs.

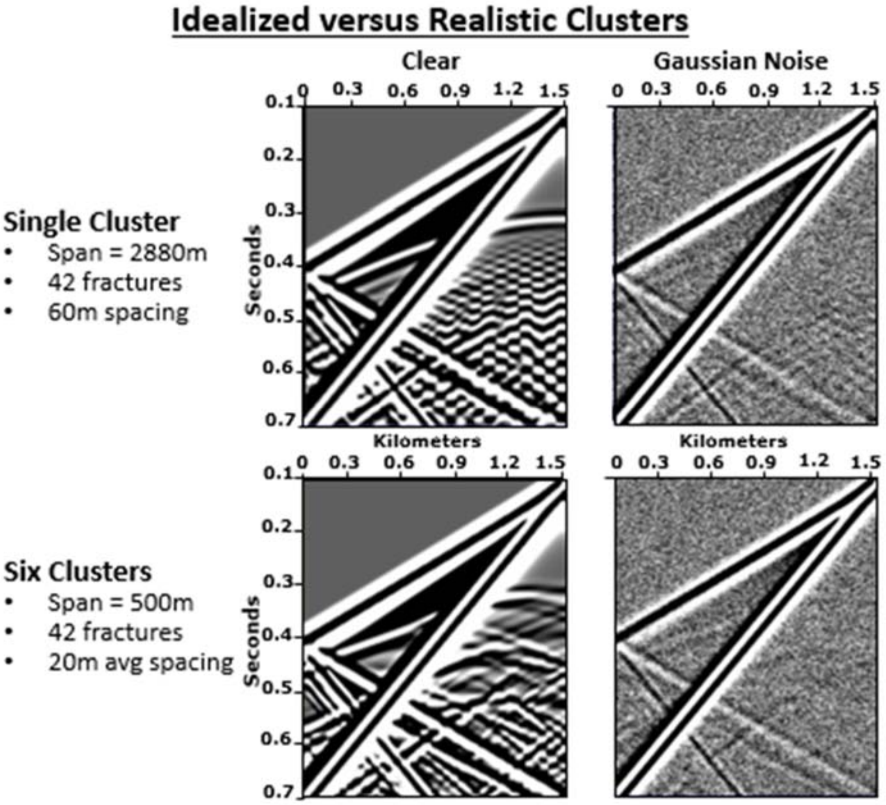

Figure 5.14: Analysis of Phase 2: Differentiation of uniform versus non-uniform fracture clustering with Gaussian noise added at a signal to noise ratio of 500:1. Though uniform fracture clustering produces distinct crosscutting energy in seismograms that is detectible with and without noise, non-uniform more realistic clusters produce little discernible pattern that hold up with the addition of noise.

SUMMARY

This chapter systematically outlines the results of the two phases of fracture network attribute alteration. Phase 1 showed that the seismic response to a single idealized fracture cluster is a regular crosscutting amplitude pattern that appears within and below the fractured interval as long as fracture spacing remains above seismic resolution. Further analysis showed that as fracture spacing decreases below one-half of the seismic wavelength, the depth at which crosscutting energy appears exponentially increases. This relationship holds until 28% of the fractures are moved from their uniformly spaced locations to random locations within the cluster. The vertical thickness of the cluster has little effect on the location or strength or the crosscutting signature. When fracture spacing decreases below seismic resolution, one fourth of the wavelength, effective reflections from the top and bottom of the fractured interval are generated.

Phase 2 showed that the seismic response to multiple realistic fracture clusters is heterogeneous anisotropy of compressional wave velocity and amplitude decay below the location of highest fracture density within each cluster. Further analysis showed that these features appear only when the ratio of fracture material to matrix material is at or greater than 3:5 within a cluster and when cluster spacing is equal to or greater than the wavelength. A summary of the sensitivity of the seismic response to fracture clustering showed that, with very little noise added, it became difficult to differentiate between uniform and non-uniform fracture clustering.

Chapter 6: Conclusions, Discussion, and Future Considerations

The specific objective of this study was to identify and analyze the seismic response to fracture clustering. Phase 1 first confirmed that the seismic response to a single idealized fracture cluster is a regular crosscutting amplitude pattern within a seismogram. As previously reported, the crosscutting pattern only appears within the fractured interval when fracture spacing is greater than the seismic resolution. Contrary to previous reports, however, crosscutting energy does not fade from the seismogram as fracture spacing decreases; rather, the energy is delayed in time and is visible below the fractured interval. Further analysis showed that as fracture spacing decreases below one-half of the seismic wavelength, the depth at which crosscutting energy appears exponentially increases. This relationship is visually detectable until approximately 28% of the fractures are moved from their uniformly spaced locations to random locations within the cluster. At this point, fracture-related seismic coda are not regularly spaced enough to constructively interfere and form a discernible crosscutting pattern. Further investigation also showed that the vertical thickness of the cluster had little effect on the location or strength or the crosscutting pattern. Lastly, Phase 1 showed that when fracture spacing decreases below seismic resolution, one fourth of the wavelength, effective reflections from the top and bottom of the fractured interval are generated within a seismogram.

The results from Phase 1 indicated that the seismic response to more natural randomly spaced fractures clustered together is not visually discernible in a seismogram. Therefore, to gain insights on multiple clusters, it was necessary to shift the focus of Phase 2 from common seismograms to wavefield snapshots that are not easily constructed from seismic surveys. Phase 2 showed, however, that the seismic response to multiple realistic fracture clusters is heterogeneous anisotropy of compressional wave velocity and amplitude decay below the location of highest fracture density within each cluster. Further analysis showed that these features appear in a wavefield snapshot only when the ratio of fracture material to matrix material is at or greater than 3:5 within a cluster and when cluster spacing is equal to or greater than the seismic wavelength. To further constrain the discernibility of the seismic response to fracture clustering, a comparison was made between the single idealized cluster of Phase 1 and the multiple more realistic clusters of Phase 2. A juxtaposition of their seismograms showed that with little noise added, it is difficult to differentiate between idealized and realistically spaced fracture clustering.

THE SEISMIC RESPONSE TO FRACTURE CLUSTERING

Although briefly covered above, it is necessary to discuss the implications of a few of the results from the phases of fracture cluster modeling. Phase 1 defined a method for determining the location and fracture density of a single cluster: measurement of the change in depth of crosscutting energy within a seismogram. This finding contradicts the results of all other studies on the subject that, instead, state that crosscutting scattered energy becomes fainter and less detectable as fracture spacing approaches seismic resolution (Pearce et al., 2003; Burns et al., 2007; Willis et al., 2004, Grandi-Karam, 2008; Xu, 2011). Their conclusions are a result of their sole focus on the fractured interval itself. Within the fractured interval, visible scattering becomes fainter but the energy has not dissipated. It is simply delayed in time. Therefore, use of the whole seismogram is important when extracting information about fracture networks with realistically small fracture spacing.

Phase 1 also showed that the vertical thickness of the cluster has little effect on the location or strength or crosscutting energy. This finding again contradicts the results of other studies that conclude that that as fractures are shortened, scattered energy increasingly attenuates (Grandi-Karem, 2008). The resulting seismic response to fracture length in this study also contradicted the hypothesized result as well. Instead of behaving in the simplistic manner diagrammed in Figure 2.3, the intensity of crosscutting energy is not a function of the number of times a ray reflects between two fractures; instead the energy is a function of the angle at which the wavefront arrives incident upon the face of a fracture. This result is counterintuitive, and it is unclear whether or not this is a numerical wave propagation approximation or a physical phenomenon.

Future Considerations

Fracture Width

The wavefield response to uniformly spaced fractures has been documented by recent authors. This study presents the same approach as outlined in the left column of Figure 4.7. However, the hyperbolic events that form at the top and bottom of each fracture within a seismogram has gone relatively unnoticed. Most other studies change the matrix velocity within the fractured interval, causing true reflections to occur where the hyperbolas align. Because a velocity change was not used in this study, the hyperbolic reflections are readily apparent and call attention to the extreme width of the fractures used in this and most other studies (Figure 5.2K and L; Figure 5.4K and L). Fracture width could potentially be responsible for the effective reflections off of the top and bottom of the fractured interval when fractures are closely spaced. Therefore, a pertinent phase that should be completed is to test the seismic response to fractures with thinner apertures. Without this knowledge, it is unclear whether or not any of the hyperbolas, mode converted S-waves, seismic coda, and therefore cross-cutting energy pattern will exist in a realistic setting. Unfortunately, this phase of fracture attribute alteration was not performed because

SWP3D could not be run in parallel and the models, otherwise, would have taken far too long to run.

Quantitative Comparison

A third phase of fracture modeling performed for this study focused on the seismic response to fracture infill. The results of this phase produced little insight into the effect that infill has on seismic waves, however. All seismograms and wavefield snapshots showed no visual contrast between gas, oil, and water-filled fractures for all variations of fracture spacing outlined in Phases 1 and 2 (e.g. Figure 6.1). There was a large decrease in the amplitude of wavefield features with cement-filled fractures but no change in the shape or locations of the events outlined in Figures 5.2 and 5.4. This feature was attributed to the fact that the calcite cement velocity closely resembled the limestone matrix velocity, whereas their densities differed measurably. The compliances used to define these fracture infills can be found in Table 4.1.

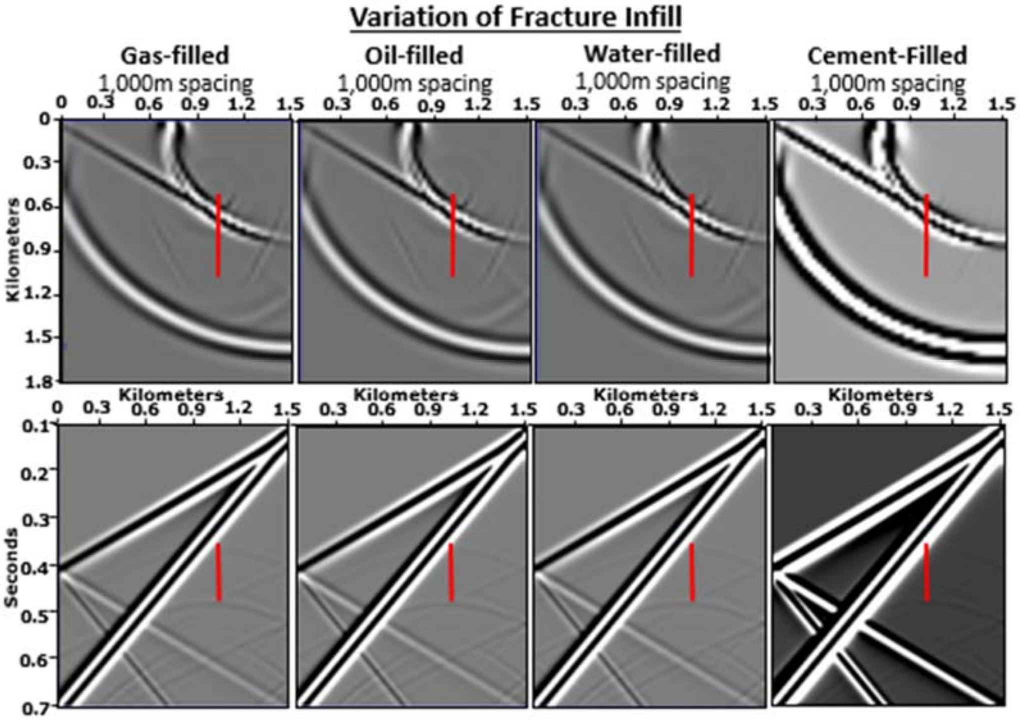

Figure 6.1: An emphasis of the difficulty in comparing the seismic response to variations in fracture infill. All models contain a cluster of 2 fractures spaced 1000m apart, though only one fracture, delineated in red, is visible in this quadrant of the model. Little if any visible difference can be discerned from fractures containing gas, oil, and water no matter the fracture density or number of clusters. Calcite cement filled fractures produce much weaker events and the right column had to be gained four times more than the others to make out the faint fracture-related events.

In order to extract more usable information when changing fracture fill, the seismogram comparison will have to be performed quantitatively instead of visually. The extraction of amplitude spectra, quality factor, and scattering index from modeled results can aid in the extrapolation of fracture network attributes from a complex wavefield (Appendix: Quantitative Measurements). Although quantitative information is pertinent to differentiating between fracture fluid types, the methods listed below could not be performed in this study in its current state for two reasons: (1) the matrix velocity within the fracture interval was not altered, preventing the formation of coherent reflections in all models from which to extract the quantitative parameters (Figure 6.2, left), and (2) the inadequate absorbing model boundaries that contaminated all but the center portion of the fractured interval with linear direct waves that are impossible to remove without altering fractured energy as well (Figure 6.2, right).

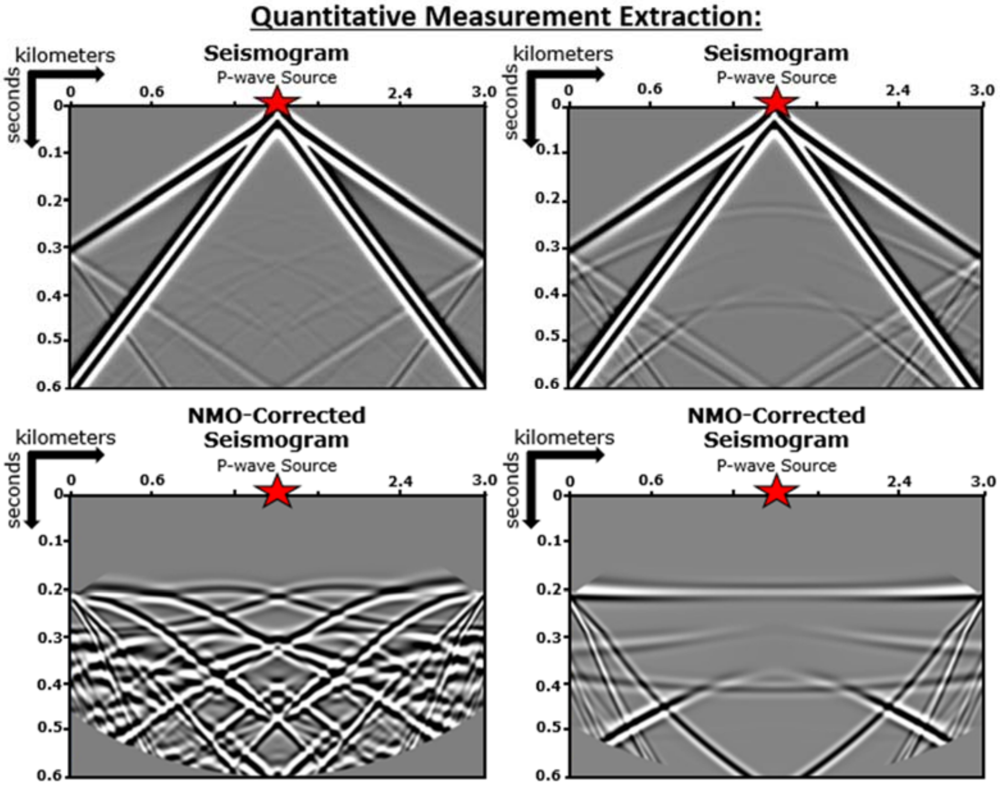

Figure 6.2: An emphasis of the difficulty in extracting quantitative measurements from reflections in moderately fractured media. The top-left image shows the unprocessed seismogram of a medium containing 6 gas-filled fractures spaced 420m apart and the resulting faint reflection hyperbolas from the top and bottom of each fracture. The bottom-left image shows the result of subtracting an isotropic seismogram from the fractured seismogram and applying NMO-correction. The top-right image shows the unprocessed seismogram of a medium containing 150 gas-filled fractures spaced 10m apart and the resulting effective reflections from the top and bottom of the fractured interval. The bottom-right image shows the result of subtracting an isotropic seismogram from the fractured seismogram and applying NMO-correction. Although the top and bottom of the fractured layer have been flattened, boundary reflections still contaminate the image.

Modeling in 3D

The last item to discuss is the benefits of modeling in 3D, which could not be performed in this study due again to the issues encountered with trying to run SWP3D in parallel. The results of this 2D study are limited to only views of wavefield events perpendicular to fracture strike. By modeling in 3D, variations can be documented parallel to fractures, perpendicular to fractures, and at any angle to fractures. This is of the utmost help when working with the faint seismogram features outlined above. Although a 2D set up allows for the study of crosscutting and scattered energy from between fractures, Figure 5.14 shows how, with a small amount of noise added to the seismograms, it becomes extremely difficult to detect these wavefield features. When modeling in 3D, seismograms perpendicular and parallel to fracture strike can be compared to highlight the fracture-related events from the background noise (Figure 2.6). Modeling in 3D could also shed light on the detectability of Phase 2 results in real seismic data. Although wavefront analysis in snapshot view is not available from seismic surveying, the phenomena of directional phase velocity variation and amplitude decay associated with heterogeneous anisotropy could be detected in seismograms produced from 3D models.

Appendix: Quantitative Measurements

The extraction of amplitude spectra, quality factor, and scattering index from modeled results can aid in the extrapolation of fracture network attributes from a convoluted wavefield. Seismic amplitude spectral analysis allows for a visual comparison of the strength of different frequency components as they vary throughout the model. A simple Fourier transform converts the time domain seismogram x(t) into its frequency spectrum X(f) and, by windowing the signal in accordance with the Short-Time Fourier Transform Method (STFT), the time dependence of frequency changes can be observed:

$$STFT(\tau,\omega) = \int_{-\infty}^{+\infty} x(t)g(t-\tau)e^{(-i\omega t)}dt\,, \tag{6.1}$$

where t is time, ω is angular frequency, τ is the time instant, and $g(t)$ is the window function (Chakraborty and Okaya, 1995). Therefore, from an amplitude spectra versus offset plot of the region below the fractured interval, it is possible to see the frequency signature of each individual fracture in space and, from the frequency shift, differentiate between differing fracture fills.

Quality factor, Q, is a measure of the amplitude decay a seismic wave undergoes as it travels through a medium. Q is the inverse of attenuation, which is caused by absorption, spherical divergence, mode conversion, viscoelastic fluid effects, and scattering (Sheriff and Geldart, 1995). The classic method for measuring Q in seismic reflection data is the Dasgupta and Clark (1998) quality factor versus offset, or QVO, method:

$$\ln\left[\frac{A(f)}{A_0(f)}\right] = 2\ln(RG) - \frac{2\pi(t-t_0)}{Q_i}f \tag{6.2}$$

$$\text{with } Q_i = \frac{t_n - t_{n-1}}{\frac{t_n}{Q_n} - \frac{t_{n-1}}{Q_{n-1}}}\,. \tag{6.3}$$

In this method, the logarithm of the ratio of recorded signal amplitude spectrum $A(f)$ to the source signal amplitude spectrum $A_0(f)$ is related to an intercept term, containing the reflection coefficient of the boundary R and the geometric spreading factor G, and a slope term, containing the record time of the two signals t and t_0, the frequency f, and the interval quality factor Q_i (Equation 6.2). To solve, the ratio of the amplitude spectra, or spectral ratio, is calculated from the seismic data and a linear regression of the logarithm of the spectral ratio against frequency gives the intercept and slope terms. Using equation 6.3, the change in quality factor, i.e. magnitude of attenuation, from the top t_0 and bottom t_n of a target interval can be determined. Using the isotropic model as a reference for background Q, the effects of fracture scattering attenuation and mode conversion can be isolated.

Scattering Index, SI, is a measure of the ringing a source wavelet develops as it travels through a fractured interval and is contaminated by coda reflections (Willis et al., 2004). In order to measure SI, two apparent source wavelets are extracted from the model by computing autocorrelations from windowed portions of the reflection time series above and below the fractured interval, representing the input $i(t)$ and output $o(t)$ wavelet, respectively.

$$i(t) * h(t) = o(t) \tag{6.4}$$

The time domain transfer function $h(t)$ is then produced by deconvolving the autocorrelation of the input wavelet from the autocorrelation of the output wavelet (Equation 6.4). A simple pulse shaped transfer function indicates that no scattering has occurred in the interval between the analysis windows, whereas a long ringing transfer function indicates extensive scattering, in this case, due to fractures. SI reduces the transfer function into one number and is essentially the moment of the transfer function:

$$SI = \sum_{i=0}^{m} |t_i| i \qquad (6.5)$$

where i is the time lag, t_i is the time domain transfer function amplitude lag at lag i, and i_m is a lag at which there is no more significant energy in the transfer function (Willis et al., 2004). Therefore, the more fractures that are present in the model, the more the transfer function will ring and the value of SI will increase.

References

Aki, K., and B. Chouet, 1975, Origin of coda waves: Source, attenuation, and scattering effects: Journal of Geophysical Research, **80**, 23, 3322-2242.

Backus, G. E., 1962, Long-wave elastic anisotropy produced by horizontal layering: Journal of Geophysical Research, **67,** 11, 4427-4440.

Bourbie, T., O. Coussy, and B. Zinszer, 1987, *Acoustics of Porous Media*: Gulf Publishing Company.

Burns, D., M. Willis, M. Toksoz, and L. Vetri, 2007, Fracture properties from seismic scattering: The Leading Edge, **26**, 1186-1196.

Chakraborty, A., and D. Okaya, 1995, Frequency-time decomposition of seismic data using wavelet-based methods: Geophysics, **60**, 6, 1906-1917.

Cheng, C. H., 1993, Crack models for a transversely isotropic medium: Journal of Geophysical Research, **98,** 675-684.

Chichinina, T., V. Sabininn, and G. Ronquillo-Jarillo, 2006, QVOA analysis: P-wave attenuation anisotropy for fracture characterization: Geophysics, **71,** C37-C48.

Coates, R. T., and M. Schoenberg, 1995, Finite-difference modeling of faults and fractures: Geophysics, **60,** 1514-1526.

Daley, T. M., K. Nihei, E. Myer, J. Queen, M. Fortuna, J. Murphy, and R. Coates, 2002, Numerical modeling of scattering from discrete fracture zones in a San Juan Basin gas reservoir: 72nd Annual International Meeting, SEG, Expanded Abstracts.

Dasgupta, R., and R. Clark, 1998, Estimation of Q from surface seismic reflection data: Geophysics, **63,** 2120-2128.

De Basabe, J. D., 2009, High-Order Finite Element Methods for Seismic Wave Propagation: PhD Thesis, University of Texas.

De Basabe, J. D., and M. K. Sen, 2009, New Developments in the finite-element method for seismic modeling: The Leading Edge, Special Section: Seismic Modeling, **28**, 562-567.

De Basabe, J. D., M. K. Sen, and M. F. Wheeler, 2011, Seismic wave propagation in fractured media: A discontinuous Galerkin approach: 81st Annual International Meeting, SEG, Expanded Abstracts.

Grandi-Karam, S., 2008, *Multiscale Determination of In Situ Stress and Fracture Properties in Reservoirs*: PhD Thesis, Massachusetts Institute of Technology.

Grechka, V., and I. Tsvankin, 1998, Feasibility of nonhyperbolic moveout inversion in transversely isotropic media: Geophysics, **63,** 957-969.

Grote, M., A. Schneebeli, and D. Schotzau., 2006, Discontinuous Galerkin finite element method for the wave equation: SIAM Journal on Numerical Analysis, **44,** 2408-2431.

Hou, S., D. Hengchang, and L. Xiangyang, 2012, Seismic response of discrete fractures: 82nd Annual International Meeting, SEG, Expanded Abstracts.

Hudson, J. A., 1980, Overall properties of a cracked solid: Mathematical Proceedings of the Cambridge Philosophical Society, **88,** 371-384.

Hudson, J. A., 1981, Wave speeds and attenuation of elastic waves in material containing cracks: Geophysical Journal of the Royal Astronomical Society, **64,** 133-150.

Hudson, J. A., E. Liu, and S. Crampin, 1996, The mechanical properties of materials with interconnected cracks and pores: Geophysical Journal International, **124,** 105-112.

Hudson, J. A., E. Liu, and S. Crampin, 1997, The mean transmission properties of a fault with imperfect facial contact: Geophysical Journal International, **129**, 720-726.

Johnson, C., 1990, *Numerical Solution of Partial Differential Equations by the Finite Element Method*: Cambridge University Press.

Leary, P. C., and R. Abercrombie, 1994, Frequency dependent crustal scattering and absorption at 5-160 Hz from coda decay observed at 2-5 km depth: Geophysical Research Letters, **26,** 1106-1111.

Marfurt, K. J., 1984, Accuracy of finite-difference and finite-element modeling of the scalar and elastic wave equations: Geophysics, **49,** 5, 533-549.

Marfurt, K. J., and R. L. Kirlin, 2001, Narrow-band spectral analysis and thin-bed tuning: Geophysics, **66,** 1274-1283.

Marrett, R., S. E. Laubach, and J. E. Olson, 2007, Anisotropy and beyond: Geological perspectives on geophysical prospecting for natural fractures: The Leading Edge, **26,** 1106-1111.

Mavko, G., T. Mukerji, and J. Dvorkin, 2009, *The Rock Physics Handbook: Tools for Seismic Analysis in Porous Media:* Cambridge University Press.

Nakagawa, S., K. Nihei, and L. Myer, 2003, Three-dimensional elastic wave scattering by a layer containing vertical periodic fractures: Journal of the Acoustical Society of America, **13**, 6, 3012-3023.

Nowak, E. J., H. W. Swan, and D. Lane, 2008, Quantitative thickness estimates from the spectral response of AVO measurements: Geophysics, **73,** C1-C6.

Oliver, J., A. E. Huespe, and I. F. Dias, 2012, Strain localization, strong discontinuities and material fracture: Matches and mismatches: Computer Methods in Applied Mechanics and Engineering, **241,** 323-336.

Oliver, P. J., 2012, *Introduction to Partial Differential Equation: (Chapter 11) Numerical Methods: Finite Elements:* University of Minnesota.

Ozkaya, S., W. Kolkman, and J. Amthor, 2003, Mechanical Layer-dependent Fracture Characteristics from Fracture Density vs. Tvd Cross Plots: Examples from Horizontal Wells in Carbonate Reservoirs, North Oman: AAPG International Conference – Barcelona, Spain.

Pearce, F., 2003: *Seismic Scattering Attributes to Estimate Reservoir Fracture Density: A Numerical Modeling Study*: M.S. Thesis, Massachusetts Institute of Technology.

Sayers, C. M., and M. Kachanov, 1991, A simple technique for finding effective elastic constants of cracked solids for arbitrary crack orientation statistics: International Journal of Solids and Structures, **6**, 671-680.

Schoenberg, M., 1980, Elastic wave behavior across linear-slip interfaces: Journal of the Acoustical Society of America, **68,** 1516-1512.

Schoenberg, M., and J. Douma, 1988, Elastic-wave propagation in media with parallel fractures and aligned cracks: Geophysical Prospecting, **36,** 571-590.

Schultz, C., and M. N. Toksoz, 1996, Experimental study of enhanced backscattering from a highly irregular, acoustic-elastic interface: Journal of the Acoustical Society of America, **99,** 880-892.

Sheriff, R. E., and L. P. Geldart, 1995, *Exploration Seismology*: Cambridge University Press.

Singh, S., H. Abu-Habbiel, B. Khan, M. Akbar, A. Etchecopar, and B. Montaron, 2008, Mapping fracture corridors in naturally fractured reservoirs: an example from Middle East carbonates: First Break, **26,** 109-113.

Spikes, K. T., 2009, Thickness estimates of heterogeneous reservoirs using seismic data, rock physics, and wavelet transforms: 79th Annual International Meeting, SEG, Expanded Abstracts, 1835-1838.

Stewart, R., J. Gaiser, R. Brown, and D. Lawton, 2002, Tutorial -- Converted-wave seismic exploration: Geophysics, **67**, 1348-1363.

Strijker, G., G. Bertotti, and S. Luthi, 2012, Multi-scale fracture network analysis from an outcrop analog: A case study from the Cambro-Ordovician clastic succession in Petra, Jordan: Marine and Petroelum Geology, **38**, 1, 104-116.

Suli, E., and D. F. Mayers, 2006, *An Introduction to Numerical Analysis,* Cambridge University Press.

Tatham, R. H., and M. D. McCormack, 1991, *Multicomponent Seismology in Petroleum Exploration,* Society of Exploration Geophysicists.

Thomsen, L., 1995, Elastic anisotropy due to aligned cracks in porous rock: Geophysical Prospecting, **43,** 805-829.

Thomsen, L., 2002, *Understanding Seismic Anisotropy in Exploration and Exploitation*: SEG Distinguished Instructor Series, No. 5.

Vlastos, S., E. Liu, G. Main, and X.-Y. Li, 2003, Numerical simulation of wave propagation in media with discrete distributions of fractures: Effects of fracture sizes and spatial distribution: Geophysical Journal International, **152,** 649-668.

Vlastos, S., 2005, *Seismic Characterization of Fluid Flow in Fractured Reservoirs:* PhD Thesis, University of Edinburgh.

Willis, M. E., F. Pearce, D. R. Burns, J. Byun, and B. Minsley, 2004, Reservoir fracture orientation and density from reflected and scattered seismic energy: EAGE Meeting Paris.

Willis, M. S., D. R. Burns, R. Rao, B. Minsley, M. N. Toksoz, and L. Ventri, 2006, Spatial orientation and distribution of reservoir fractures from scattered seismic energy: Geophysics, **71,** O43-O51.

Worthington, M. H., and R. Lubbe, 2007, The scaling of fracture compliance: Geological Society of London, Special Publications, **270**, 73-82.

Xiao, L., and K. Li, 2011, Characteristics of the nuclear magnetic resonance logging response in fracture oil and gas reservoirs: New Journal of Physics, **13**, 1367-2630.

Xu, Y., 2011, *Analysis of P-wave Seismic Response for Fracture Detection: Modeling and Case Studies:* PhD Thesis, University of Edinburgh.

Zhang, J., 2005, Elastic wave modeling in fractured media with an explicit approach: Geophysics, **70,** T75-T78.

Zhang, Y., C. M. Sayers, and J. I. Adachi, 2009, The use of effective medium theories for seismic wave propagation and fluid flow in fractured reservoirs under applied stress: Geophysical Journal International, **177,** 205-221.

Vita

Lauren Becker was born in Slidell, Louisiana, USA in 1989. She moved to Houston, Texas, USA with her family in 2003 and attended Westside High School. Upon graduating in 2008, she attended the University of Texas at Austin, where she earned a Bachelor of Science in Geological Sciences with an option in geophysics in 2012. After a summer internship with Cabot Oil and Gas Corporation in Houston, she continued her education as a graduate student again at the University of Texas at Austin. While in graduate school, she completed a summer internship with Marathon Oil Company in Houston. She graduated with a Master of Science in Geological Sciences with an emphasis in geophysics the following summer of 2014. She accepted a full time position as a geophysicist with BP and began work at their Houston office after graduating.

Permanent email: lau.beck12@gmail.com

This thesis was typed by the author.